

**This item is the archived peer-reviewed author-version of:**

Single layer graphene controlled surface and bulk indentation plasticity in copper

**Reference:**

Bahrami F., Hammad M., Fivel M., Huet B., D'Haese C., Ding Lipeng, Nysten B., Idrissi Hosni, Raskin J.P., Pardoen T..- Single layer graphene controlled surface and bulk indentation plasticity in copper  
International journal of plasticity - ISSN 0749-6419 - 138(2021), 102936  
Full text (Publisher's DOI): <https://doi.org/10.1016/J.IJPLAS.2021.102936>  
To cite this reference: <https://hdl.handle.net/10067/1767290151162165141>

# Single layer graphene controlled surface and bulk indentation plasticity in copper<sup>1</sup>

F. Bahrami<sup>a,b</sup>, M. Hammad<sup>a,b</sup>, M. Fivel<sup>c</sup>, B. Huet<sup>b</sup>, C. D'Haese<sup>d</sup>, L. Ding<sup>e, f</sup>, B. Nysten<sup>d</sup>, H. Idrissi<sup>a,e</sup>, J.P. Raskin<sup>b</sup>, T. Pardoen<sup>a</sup>

<sup>a</sup> Institute of Mechanics, Materials and Civil engineering (iMMC), Université catholique de Louvain (UCLouvain), B-1348 Louvain-la-Neuve, Belgium

<sup>b</sup> Information and Communication Technologies, Electronics and Applied Mathematics (ICTEAM), Université catholique de Louvain (UCLouvain), B-1348 Louvain-la-Neuve, Belgium

<sup>c</sup> Univ. Grenoble Alpes, CNRS, Grenoble INP, SIMaP, 38000 Grenoble, France

<sup>d</sup> Institute of Condensed Matter and Nanosciences – Bio-and Soft Matter (IMCN/BSMA), Université catholique de Louvain (UCLouvain), B-1348 Louvain-la-Neuve, Belgium

<sup>e</sup> Electron Microscopy for Materials Science (EMAT), Department of Physics, University of Antwerp, Groenenborgerlaan 171, B-2020, Belgium

<sup>f</sup> Key laboratory for Light-weight Materials, Nanjing Tech University, Nanjing 211816, PR China

---

## Abstract

The impact of graphene reinforcement on the mechanical properties of metals has been a subject of intense investigation over the last decade in surface applications to mitigate the impact of tribological loadings or for strengthening purposes when dispersed into a bulk material. Here, the effect on the plastic indentation response of a single graphene layer grown on Cu is analysed for two configurations: one with graphene at the surface, the other with graphene sandwiched under a 100 nm thick Cu cap layer. Nanoindentation under both displacement and load control conditions show both earlier and shorter pop-in excursions compared to systems without graphene. Atomic force microscopy reveals much smoother pile-ups with no slip traces in the presence of a surface graphene layer. The configuration with the intercalated graphene layer appears as an ideal elementary system to address bulk hardening mechanisms by indentation testing. Transmission electron microscopy (TEM) cross-sections below indents show more diffuse and homogeneous dislocation activity in the presence of graphene. 3D dislocation dynamics simulations allow unraveling of the origin of these 3D complex phenomena and prove that the collective dislocation mechanisms are dominantly controlled by the strong back stress caused by the graphene barrier. These results provide a quantitative understanding of the impact of graphene on dislocation mechanisms for both surface and bulk applications, but with an impact that is not as large as anticipated from other studies or general literature claims.

*Keywords:* Graphene, nanoindentation, plasticity, dislocation dynamics, contacts

---

<sup>1</sup> Published in [International Journal of Plasticity 138 \(2021\) 102936](#)

## **Introduction**

Graphene (Gr) possesses superior mechanical properties (Choi et al., 2010; Ovid'ko, 2013) which can improve the tribological performance of materials when used as surface coating and/or the bulk strength and stiffness when used as reinforcement in composites or as an interface in multilayers (Kim et al., 2013; Li et al., 2018; Park et al., 2017). These claimed beneficial impacts on mechanical behaviour add to the extra functionality resulting from the insertion of graphene in terms of electrical, thermal, or optical performances (Nieto et al., 2017; Porwal et al., 2013).

The composite effect has been demonstrated for polymer-based (Lahiri et al., 2011; Ni et al., 2008) and a few metal-based (Nieto et al., 2017; Tjong, 2013) nanocomposites, although at the expense often of ductility. In metals, the strengthening mainly originates from the impenetrability by dislocations of the metal-graphene interface similar to a strong grain boundary (Hwang et al., 2013; Kim et al., 2013). The high strength of graphene allows building up very large stress without failure and dislocation penetration. These mechanisms have been studied both experimentally and numerically (Bartolucci et al., 2011; Chen et al., 2012; Dorri Moghadam et al., 2015; Kuang et al., 2013; Tjong, 2013). For instance, an enhanced strength in Cu/Gr laminates has been attributed to dislocation piling up at the Cu and graphene interface (Kim et al., 2013). A Cu/Gr nanolayered composite deformed by shear exhibits improved toughness and shear strength in comparison to pure metal (Liu et al., 2016).

Regarding surface effects, one of the most convenient ways to determine the local resistance to a mechanical contact is by nanoindentation with the potential to quantify the elastic stiffness and plastic strength (or hardness) for penetration depth at nanometer scale (Jian et al., 2010; Pharr and Oliver, 1992). From the viewpoint of elasticity, the stiffer response of Gr-coated Cu has been demonstrated through experimental and theoretical studies (Hammad et al., 2017). This stiffening was found to result from the adhesionless contact between the nanoindenter and

the graphene layer more than from a direct effect of graphene's high elastic modulus. The graphene layer acts thus as a shielding layer suppressing the adhesive forces and leading to an elastic response in almost perfect agreement with Hertz theory. The higher elastic modulus of Gr-coated Cu compared to Gr-free Cu was confirmed by Park et al. using also nanoindentation (Park et al., 2019). Klemenz et al. showed that Pt can resist higher loads in the presence of graphene coating for shallow indentation depth (Klemenz et al., 2014).

From the viewpoint of plasticity during indentation, plasticity initiates by punching out dislocations when indenting almost defect-free regions of metallic crystals (Jian et al., 2010). When the maximum shear stress under the indenter reaches the theoretical shear stress, a discrete avalanche of dislocations is triggered causing the so-called "pop-in" excursions in the load-displacement curve (Gouldstone et al., 2000; Sato et al., 2019). The length of a pop-in is directly proportional to the number of dislocations involved in the avalanche (Suresh et al., 1999). A few studies recently addressed the plastic response of Gr-covered metallic materials. Molecular dynamics simulations of nanoindentation on Cu coated with single layer graphene have shown an improved strength due to the modification of the dislocation activity near the Cu/Gr interface (Zhu et al., 2019). The plastic response of Cu/Gr under indentation has recently been investigated by Zhu et al., finding larger and later pop-in excursions when compared to bare Cu (Zhu et al., 2019). However, in the other recent investigation by Park et al. on the same system, pop-in excursions were found to be smaller and earlier in the presence of graphene (Park et al., 2019). Aside from the different trends observed in these two studies, open questions remain regarding the fundamental origin of the change of pop-in length in the presence of graphene, about the statistical analysis of the phenomena, and about the reasons explaining why graphene affects the onset of plasticity. Also, questions may be raised about possible artefacts coming from the use of a load control mode with respect to the unstable pop-in mechanism which cannot be properly resolved due to possible overshoot of the unstable pop-in penetration

increment. Furthermore, no study has reported the interest of using indentation to study interface controlled plasticity effects with a small cap layer above the graphene layer.

The objective of this study is to investigate the effect of graphene on the contact plasticity when graphene is either coating a Cu substrate or buried under a thin cap layer made also of Cu (but with a much smaller grain size). More precisely, highly crystalline single-layer graphene is directly grown on Cu by chemical vapor deposition (Huet and Raskin, 2018a, 2017). Using as-grown graphene circumvents the transfer process, which inevitably leads to graphene degradation and contamination. Moreover, the adhesion between CVD-grown graphene and the underlying Cu film is larger than for transferred Gr. The plastic response and underlying dislocation mechanisms are carefully studied by comparing four distinct systems: (i) annealed Cu film (as referred to as  $Cu_A$ ) (ii) graphene as grown on Cu film ( $Cu_A/Gr$ ), (iii) a 100 nm-thick Cu film directly evaporated on an annealed Cu film ( $Cu_A/Cu_N$ ), (iv) a 100 nm-thick Cu film directly evaporated on as-grown graphene ( $Cu_A/Gr/Cu_N$ ). In order to understand better the root causes of the observed effects on the plastic flow, transmission electron microscopy (TEM) is used to compare samples after nanoindentation in terms of dislocation structures. Atomic force microscopy (AFM) provides additional pieces of evidence regarding the impact of graphene on the development and the localization of the plastic flow. Furthermore, 3D discrete dislocation dynamics (DDD) simulations are conducted to unravel more quantitatively how dislocations interact and multiply under the indent with and without the presence of graphene. This system offers a unique opportunity for direct comparisons of a 3D DDD framework on experimental results.

The paper starts with the presentation of the materials and test procedures in section 2 and is followed by section 3 including the results of nanoindentation in two different modes for the studied systems as well as all the other characterization and modelling results. Finally, section 4 provides a discussion followed by the conclusions.

## 2. Materials and test procedures

### 2.1 Materials

Cu substrates are produced by electron beam evaporation of 99.999% pure Cu pellets (Kurt J. Lesker) on 3 in. fused quartz wafers. The 1200 nm-thick Cu film is deposited at room temperature with a 4 Å/s under a base vacuum of about  $2 \times 10^{-7}$  mbar. The Cu film then serves as a catalyst for the synthesis of single-layer graphene, which takes place at about 1050°C under an atmosphere composed of methane, hydrogen, and argon. Additional Cu film substrates have been annealed under the same thermal protocol using only an Ar/H<sub>2</sub> atmosphere in order to obtain a Cu sample with similar purity and microstructure but without any graphene. The CVD process is described somewhere else in detail (Huet and Raskin, 2018a; Huet et al., 2019). For the final step of sample preparation, a Cu film with 100 nm thickness (Cu<sub>N</sub>) has been deposited by evaporation on top of each type. Fig. 1 represents a schematic of the tests samples including (a) a bare annealed copper substrate (Cu<sub>A</sub>), (b) a graphene-coated copper substrate (Cu<sub>A</sub>/Gr), (c) an annealed copper substrate covered by a thin nanocrystalline copper layer (Cu<sub>A</sub>/Cu<sub>N</sub>), and (d) a graphene-coated copper substrate covered by nanocrystalline copper cap layer (Cu<sub>A</sub>/Gr/Cu<sub>N</sub>).

### 2.2 Test procedures

#### 2.2.1 Structural and microstructural analysis

Raman spectroscopy (LabRAM HR by Horiba, excitation energy: 2.41 eV/514 nm, spot size: 1 μm) has been used in order to characterize the as-grown graphene on the Cu substrate.

The grain characteristics of the Cu<sub>A</sub> and Cu<sub>N</sub> films have been characterized by scanning electron microscopy (SEM) (Zeiss Gemini Ultra-55) which also allowed positioning the indents with respect to the grain boundaries. Two types of detectors have been used an in-lens and a regular Everhart-Thorney (E-T). EHT (electron high tension) and working distance were 2 kV

and 4 mm respectively. Electron backscatter diffraction (EBSD) relying on a MEB FEG ZEISS GeminiSEM500 with an EBSD camera CCD Hikari Super 1400pts/s EDAX) was used to determine the crystallographic texture.

AFM mapping (Dimension Icon Instrument by Bruker, standard tapping mode in air, linear scanning rate: 0.5 Hz) has been performed to collect images of the surface before indentation as well as of the indents in order to compare the topography and to determine the height of the pile-ups. Non-contact silicon probes (Nanosensors, PPP NCHR) have been used with nominal spring constant 40 N/m and tip radius <10 nm.

Cross-sectional TEM thin films have been prepared under the indents using a dual-beam focused ion beam (FIB) instrument (FEI Helios Nanolab 650). Electron beam followed by ion beam deposition of Pt layers was used in order to protect the surface of the film during FB thinning. Bright-field images have been taken with an FEI Tecnai G2 F20 transmission electron microscope operated at 200kV in order to analyze the dislocation structures and decohesion/failure events at interfaces.

### *2.2.2 Nanoindentation*

Two different nanoindentation devices were used in order to determine the load-penetration responses and cross-validate the delicate measurements of pop-in lengths taking place at very small penetration depth. A pop-in involves an avalanche of dislocations, which is a dynamic phenomenon. Hence, during a pop-in under load control conditions, the indenter is abruptly losing contact with the surface and the indenter tip is suddenly accelerated. When the tip gets again in contact with the surface, equilibrium is not reached instantaneously and, due to inertia, an extra penetration is thus possible. The unstable nature of the pop-in under load control mode may thus lead to an overestimation of the pop-in length. Hence, displacement control experiments, which are less commonly used, have also been performed with another equipment. Under displacement control, a decrease of the force is allowed, stabilizing the response during

a pop-in event. Independently of the application of two different loading modes, the use of two devices also provides a more robust basis of results for the analysis.

The load-controlled test campaigns were performed with the Agilent nanoindenter relying on the continuous stiffness measurement (CSM) mode at a representative strain rate of  $0.05 \text{ s}^{-1}$  and on the use of a diamond Berkovich tip. The radius of the tip has been measured as equal to  $\sim 40 \text{ nm}$  by scanning electron microscopy (Ultra-55 from Zeiss) and the tip was calibrated on a standard silica sample with a known Young's modulus equal to  $72 \text{ GPa}$ . More than 300 indents have been performed with the Agilent system in order to generate statistically valid data.

The displacement-controlled tests have been performed with a UNHT<sup>3</sup> Anton Paar system including a feedback loop on the applied force signal. In this case, the displacement is calculated from the relative altitude measured between the indenter and a reference sphere in contact with the surface. This gives a theoretically infinite stiffness to the system avoiding any stiffness correction to cancel thermal drift. A diamond Berkovich tip was used, with a radius of curvature equal to  $\sim 100 \text{ nm}$ .

### *2.2.3 Discrete dislocation dynamics (DDD) simulations*

The 3D DDD setup has been described in several references (Fivel, 2008; Verdier et al., 1998). It combines a DDD code (TRIDIS) which solves the dislocation kinetics and equilibrium, and a Finite Element (FE) code (CAST3M, FE Software available at [www-cast3m.cea](http://www-cast3m.cea)) in order to treat full boundary value problems. Such a combination is required in the case of nanoindentation simulations in order to consider the heterogeneous stress induced by the indenter correctly and to account for the image forces associated with the indented free surface. Only the  $\text{Cu}_A$  and  $\text{Cu}_A/\text{Gr}$  systems have been modelled.

The nanoindentation test has been simulated by applying force with a rigid spherical punch to penetrate through small displacement increments inside the solid. After each displacement increment, several iterations are necessary to reach a state of equilibrium for the dislocations in



the box. The Cu substrate is described through its elastic constants assuming elastic isotropy ( $E = 112$  GPa,  $\nu = 0.324$ ). For the graphene layer, a purely elastic ( $E = 1000$  GPa,  $\nu = 0.19$ ) row of elements is introduced sharing common nodes with the Cu solid assuming perfect adhesion. The validity of this assumption of good adhesion for the case of graphene grown on Cu has been indirectly verified in previous work based on molecular dynamics simulations (Hammad et al., 2017). In the DDD framework, a strong planar interface is introduced to reproduce the presence of the Gr layer. In the simulations reported in this paper, a perfect interface is considered, but a stress-based decohesion criterion can also be taken into account.

The DDD framework also requires the introduction of dislocation sources in order to initiate the dislocation multiplication process. Thus, empirical choices had to be guided by the physics of the problem. The simulations are conducted in a quasi-static loading mode; the indenter position is changed after the dislocation microstructure is fully relaxed. The relaxation condition is based on the rate of changes of the indentation force: equilibrium position is assumed when the force did not change by more than 0.1% between 10 consecutive dislocation dynamic computation steps. A convergence analysis has been carefully performed to ensure that the response is independent of the way the loading is applied, and of the number of introduced prismatic loops. This led to the number of prismatic loops introduced to be equal to 8 sets of three interstitial loops and their corresponding 24 vacancy loops. Molecular dynamic (MD) simulations of nanoindentation in (111) oriented Cu crystal have shown (Chang et al., 2010; Fivel, 2011) that nucleation occurs through the inoculation of a first defect below the surface, just beneath the indenter, which quickly degenerates into three prismatic loops. These prismatic loops correspond to three interstitial loops built on the three  $\langle 110 \rangle$  directions, which are not included in the surface plane (see Figure 2). The size of the loops is defined by the radius of the contact area,  $R_c$ , at a given penetration depth. Note that the presence of prismatic loops for low penetration indentation has been confirmed experimentally for FCC metals by TEM

observations in 316L stainless steel (Fivel et al., 1998). In previous studies (Chang et al., 2010), this nucleation process has been successfully introduced in the DD code, and spherical indentation on a (111) Cu single crystal (in agreement with the experimental texture (Huet and Raskin, 2018b) was performed. It is shown that the dislocation microstructure evolution followed two regimes. The artificially inserted interstitial dislocation loops are initially gliding along with their cylinder similar to what is predicted by the MD simulations. Since the loop size is proportional to the contact radius, the loops get larger with increasing penetration depth and, at some point; their size gets large enough for the Frank-Read mechanism to operate on each arm of the loop, leading to a dislocation avalanche and a large increase of the dislocation density. After this stage, the induced dislocation density is capable to perfectly accommodate the spherical shape of the indenter without any need for additional dislocation nucleation events. Hence, in the present study, the same procedure has been used to initiate the plasticity mechanisms with a specific focus on the strain bursts induced by the dislocation nucleation process. The main differences with the previous study are: (i) the radius of the indenter tip is equal to 40 nm in order to match with the experiments; (ii) the nucleation process is triggered at a pre-defined penetration depth equal to 5, 10, 15 or 20 nm in order to check the effect of the penetration depth on the size of the strain bursts; (iii) the nucleation mechanism consists of a sufficiently large number of prismatic loops, typically 8 per activated Burgers vector, such that the dislocation dynamics process is already in the avalanche regime; (iv) in the case of the Cu<sub>A</sub>/Gr system, an impenetrable surface (facet) is introduced at the interface between the Cu substrate and the graphene layer; (v) for each inserted interstitial prismatic loop, there exists an equivalent vacancy loop located on the same cylinder but closer to the graphene layer in the case of Cu<sub>A</sub>/Gr and outside the simulated volume in the case of Cu<sub>A</sub>. This has been imposed in order to trigger a mechanism with no mass loss and to ensure the consistency of the calculation of the surface steps as demonstrated in (Fivel and Depres, 2014).

### 3. Results

#### 3.1 Experimental results

##### 3.1.1 Characterization of structure and microstructure

Figure 3 shows the Raman spectrum obtained for the graphene on  $\text{Cu}_A/\text{Gr}$  sample. A high 2D-to-G peak intensity ratio and narrow 2D bandwidth (larger than 2 and  $20 \text{ cm}^{-1}$ , respectively) prove the single atomic layer nature of the graphene. In addition, the D-to-G peak intensity ratio is smaller than 0.1, which indicates a low density of structural defects in as-grown graphene.

Figs. 4a and 4b compare SEM micrographs of the surface of the  $\text{Cu}_A$  and  $\text{Cu}_N$  films. The  $\text{Cu}_A$  exhibits relatively large grains in the 10 to 100  $\mu\text{m}$  range, as a result of the high temperature annealing associated with the graphene growth process. This large grain size will avoid possible artefacts from the interaction between the plastic size below the indent with the constraint associated with the grain boundaries (see further). The  $\text{Cu}_N$  film has a grain size in the 50 to 100 nm range (which cannot be clearly seen on a SEM image but confirmed by TEM analysis, see further), commensurate with the thickness as commonly observed with thin metallic films. Figures 4c and 4d provide EBSD maps and pole figures, respectively, of a  $\text{Cu}_A$  film revealing the expected sharp (111) texture.

##### 3.1.2 Indentation of $\text{Cu}_A$ and $\text{Cu}_A/\text{Gr}$

Fig. 5 is an SEM micrograph showing a set of indents inside a  $\text{Cu}_A$  grain. Only indents produced sufficiently far from the grain boundaries were kept for further analysis in order to avoid specific interaction effects between dislocations and grain boundaries, which may convolute with the interactions with the graphene layer. Furthermore, the indents were all made in (111) grains, avoiding the effect of crystallographic orientation on the plastic indentation response (Britton et al., 2010; Selvarajou et al., 2014).

Figures 6a and 6b show representative load-penetration curves for the  $\text{Cu}_A$  and  $\text{Cu}_A/\text{Gr}$  systems as measured under load-controlled and displacement-controlled conditions, respectively. The pop-in produced under load-control leads to a plateau associated with a sudden finite penetration (Fig. 6a with a zoom on the pop-ins) while it leads to a force drop which involves some extra displacement due to the non-instantaneous feedback loop operation under displacement-control mode. In the last case, the pop-in length is determined to be equal to the displacement difference from the load drop point to the point at which the load increases back to the same value as before the drop shown in Fig. 6b. The differences in the elastic response between bare Cu and Cu/Gr as well as on result of a Hertzian analysis of the elastic regime have already been investigated in depth by Hammad et al. (Hammad et al., 2017), see the introduction. The focus in this work is on the initiation of plasticity and pop-in events detected in each load-penetration curve which have been systematically analysed in order to determine the quantitative effect of graphene on the elastoplastic indentation response of the Cu layer. More than one pop-in is observed in most load-displacement curves. In the case of  $\text{Cu}_A$ , second pop-ins rarely occur and third pop-ins are never observed as shown in Fig 6c. However, in  $\text{Cu}_A/\text{Gr}$  system, besides the first and second pop-ins, third pop-ins frequently occur as can be observed in Fig. 6d. Fig. 6e shows variations of the pop-in length as a function of the load at the onset of the pop-in in  $\text{Cu}_A$  and  $\text{Cu}_A/\text{Gr}$  systems under load control mode. The comparison of the collections of first and second pop-ins in  $\text{Cu}_A$  with first, second and third pop-ins in  $\text{Cu}_A/\text{Gr}$  shows that, in the case of  $\text{Cu}_A$ , the pop-in length increases with the load whereas it remains relatively constant in  $\text{Cu}_A/\text{Gr}$  system. Figures 6f and 6g provide the variations of the first pop-in length as a function of the critical load at the onset of the plastic burst of more than 300 indents, for the  $\text{Cu}_A$  and  $\text{Cu}_A/\text{Gr}$  systems in load-control and displacement-control modes, respectively. The results are similar under both conditions with less dispersion in displacement-control mode. The load at the onset of plasticity is on average

smaller in the case of the  $\text{Cu}_A/\text{Gr}$  system compared to the bare  $\text{Cu}_A$ . Finally, Figs. 6h and 6i plot the probability function of pop-in lengths in different ranges as a function of load for the load-control and displacement-control conditions, respectively.

### *3.1.3 Indentation of $\text{Cu}_A/\text{Cu}_N$ and $\text{Cu}_A/\text{Gr}/\text{Cu}_N$*

All tests made on the sandwich configurations were performed under load-controlled mode using the Agilent nanoindenter, based on the earlier validation that both loading modes provide similar pop-in behaviour. The indents have been characterized first by SEM to verify the absence of cracks in the  $\text{Cu}_N$  films. Due to the nanocrystalline nature and the expected high strength / low ductility behaviour, there was indeed a possibility of indentation-induced damage and cracks that we had to discard. Figure 7a shows the comparison of two representative load-displacement curves for the  $\text{Cu}_A/\text{Cu}_N$  and  $\text{Cu}_A/\text{Gr}/\text{Cu}_N$  systems. The comparison of pop-in length in Fig. 7b indicates the clear influence of the graphene interlayer on the pop-in length. The pop-in length is significantly reduced in the presence of a graphene layer. The difference is clearly stronger than for the  $\text{Cu}_A/\text{Gr}$  versus  $\text{Cu}_A$  systems.

### *3.1.4 Indentation of $\text{Cu}_A$ and $\text{Cu}_A/\text{Cu}_N$*

Figure 8 provides a comparison of 5 randomly chosen load-penetration curves for the  $\text{Cu}_A$  and  $\text{Cu}_A/\text{Cu}_N$  systems. It reveals a significant difference in the length of the first pop-in when comparing these two systems. The pop-in occurs at a much larger depth in the  $\text{Cu}_A/\text{Cu}_N$  system, which is an indication that the pop-in is induced by a plastic burst taking place inside the  $\text{Cu}_A$  substrate. Furthermore, the zoom on the  $\text{Cu}_A/\text{Cu}_N$  system shows many small pop-ins before the first large one.

As a useful information for further interpreting the indentation data on the systems with the  $\text{Cu}_N$  cap layer, Figure 9 shows the variation of the hardness extracted using the Oliver and Pharr method as a function of penetration depth (Oliver and Pharr, 1992). After a regime dominated

by the elastic and elastoplastic transition, the hardness of the  $\text{Cu}_N$  is found to be  $\sim 2.5$  GPa. Deeper indentation leads to a response dominated by plasticity inside the  $\text{Cu}_A$  substrate with a hardness converging towards the  $\text{Cu}_A$  hardness, near 1.4 GPa.

### 3.1.5 AFM investigation

Figs. 10a and 10b compare the initial surface topography of  $\text{Cu}_A$  and  $\text{Cu}_A/\text{Gr}$  systems before indentation. The surface in the presence of graphene exhibits a finer topography. This is in agreement with other observations in the literature, which indicate the existence of Cu steps-terraces/step bunching under graphene. It is explained in (Kang et al., 2016; Yi et al., 2018) that Cu atoms re-arrange underneath graphene during the high-temperature CVD process in order to minimize the compressive strain or the local bending energy in graphene. The deep black lines marked in the figures correspond to the grain boundaries.

Figures 10c-f provide AFM images of the indented regions in order to characterize the differences between systems with and without graphene. Some indents show higher penetration depth, which could result from the existence of some defects in the  $\text{Cu}_A$  surface below the indenter. However, these indents have been discarded from the analysis.

Small patterns (particle-like) are observed especially around the indents on the  $\text{Cu}_A$  samples while they are not observed on the  $\text{Cu}_A/\text{Gr}$  one. Analysis of the height profiles across the indents (Fig. 10g-j) shows that the presence of graphene induces significantly smaller pile-ups. The use of AFM to characterize pile-ups has been validated in the literature (Kese and Li, 2006; Moharrami and Bull, 2014). On the other hand, the comparison of the AFM profiles for the  $\text{Cu}_A/\text{Gr}/\text{Cu}_N$  versus  $\text{Cu}_A/\text{Cu}_N$  systems does not reveal significant variation.

### 3.1.6 TEM characterization

TEM micrographs after indentation down to 200 nm depth reveal the difference between dislocation arrangements in  $\text{Cu}_A$  and  $\text{Cu}_A/\text{Gr}$  systems under indents (Figs. 11a-b). The

formation of dislocations walls in the  $\text{Cu}_A$  system and the much more spread and homogenous distribution of dislocations in the  $\text{Cu}_A/\text{Gr}$  system is a signature of the influence of the graphene barrier on dislocation activity. Figs. 12a-b show TEM micrographs of the dislocation microstructure in the  $\text{Cu}_A/\text{Cu}_N$  and  $\text{Cu}_A/\text{Gr}/\text{Cu}_N$  systems for 100 nm indentation depth where the main pop-in has already occurred. Performing a TEM characterization on a section corresponding to 100 nm indentation depth, i.e. just after the first pop-in, was chosen to limit the distortion of the interface with the graphene layer and to make easier the characterization. The system with graphene requires a higher force for inducing almost the same pop-in length (see Fig. 12c). A high density of dislocations is stored against the graphene barrier. The root cause of this phenomenon will be discussed in the next section.

Many TEM observations show local failure events at the level of the graphene layer after indentation. This can be due to graphene fracture and/or decohesion. Some evidences can be seen in Fig. 11b in the form of a white band at the level of the graphene boundary in the system  $\text{Cu}_A/\text{Gr}$ . The size of this white band is made larger due to the presence of some fragments of the Cu films under the indent, which hinders a good cohesion between the electron beam deposited Pt layer and the Cu film. It can thus be concluded that the white band in Fig. 11b is due to the presence of fragments of graphene under the indent. Fig. 13 shows a more obvious example of decohesion for the  $\text{Cu}_A/\text{Gr}/\text{Cu}_N$  system in a micrograph taken under the high-angle annular dark-field scanning TEM (HAADF-TEM) imaging mode. Still, care should be taken in the interpretation of the micrograph of Fig. 13 as there is no full guarantee that decohesion is between the  $\text{Cu}_A$  layer and graphene, and not between the  $\text{Cu}_N$  layer and graphene.

### *3.2 DDD results*

Figure 14 shows the force-penetration curves computed by DDD in the case of  $\text{Cu}_A$  and  $\text{Cu}_A/\text{Gr}$  for different values of the critical depth to trigger the nucleation process. The case of  $\text{Cu}_A$  is plotted in Figure 14a. The mechanical response starts with an elastic response, which follows

the Hertz model. After dislocation nucleation, the elastic loading curve shifts to a plastic master curve which nicely matches the experiments. A higher critical load at nucleation leads to a higher pop-in length as measured experimentally. This is a direct signature of the transition from the Hertz regime to the plastic regime.

Figure 14b shows that in the case of Cu<sub>A</sub>/Gr, the spreading of the pop-in length is significantly reduced in agreement with the experiments. However, the plastic curve after nucleation does not match well with the experiments as a stiffer response is predicted by the DDD simulations. This discrepancy will be discussed in the next section.

Figure 15 shows the dislocation arrangements as well as the density of the dislocations computed in a cubic box of size 5 x 5 x 5 μm<sup>3</sup> for both systems at different instants of the indentation process in the case of a nucleation process triggered at 10 nm depth. The full movies are available at (<http://www.numodis.fr/tridis/cugraphene.html>). The dislocation densities are similar until a penetration depth of 30 nm and then the density increases a lot more in the case of Cu<sub>A</sub>/Gr. For a penetration depth of 60 nm, the Cu<sub>A</sub>/Gr system contains four times more dislocations than the Cu<sub>A</sub>. There is a marked difference between the arrangement of the dislocations. The plastic zone, corresponding to the zone with the highest dislocation density is contained in a sphere in the case of Cu<sub>A</sub> whereas it expands as a half sphere in the case of Cu<sub>A</sub>/Gr with a larger volume and more delocalized plastic flow. This difference in the dislocation arrangement is correlated to the indentation force, which is found to be higher in the presence of graphene. In order to illustrate the back force induced by the dislocations on the indenter, we have plotted in Figure 16 the normal component of the internal stress field generated by the dislocations as if they were in an infinite medium. This highlights the much stronger long-range field development in the case of the Cu<sub>A</sub>/Gr system compared to Cu<sub>A</sub>.



## 4. Discussion

### 4.1 $Cu_A$ versus $Cu_A/Gr$ systems

The results presented in section 3 confirm the earlier finding described in the literature (Kim et al., 2013; Liu et al., 2016; Park et al., 2019; Zhu et al., 2019) that the presence of single layer graphene affects the development of the plastic flow. The effect of the presence of graphene requires a sufficient adhesion between the graphene and the substrate and results from the very large strength of graphene, which can support extreme stresses and distortions without fracture. However, the present study brings about both new elements of discussion, some more nuanced interpretations as well as some mitigated claims regarding the true potential of graphene to increase the strength of surfaces.

When comparing the elastic response of  $Cu_A$  and  $Cu_A/Gr$  after indentation in Fig. 6a, we confirm the enhancement of the load to be imposed to reach the same indentation depth for the  $Cu_A/Gr$  system, as shown in the zoom of Figure 6a for penetration depths below 10 nm, before first pop-ins, and reported by other researchers (Hammad et al., 2017; Park et al., 2019). The underlying reason is, as explained in the introduction, the adhesionless contact between the tip of the indenter and the surface in the presence of graphene, and not a stiffening effect related to the high elastic modulus of graphene. The adhesion force between the tip and the surface in the case of bare Cu modifies the contact area and the load transfer. The absence of adhesion between the indenter tip and the surface in the  $Cu_A/Gr$  system makes the tip exert the entire load required to achieve the same indentation depth, leading to higher applied forces (Hammad et al., 2017).

Nevertheless, the core of this study is on the plastic response under mechanical contact. When indenting a material with a sufficiently low density of defects, the first plastic event is caused by the nucleation, glide, and an avalanche of dislocations (Corcoran et al., 1997; Gouldstone et al., 2000; Sato et al., 2019; Suresh et al., 1999). This avalanche leads to a

displacement-burst under load-control. A proportional relationship between the pop-in length and the critical load is expected for metals, as elaborated by Shibutani (Shibutani et al., 2007). These authors worked out a relationship showing that the pop-in length increases linearly with load because a proportional number of dislocations is required to release the increasing stored elastic energy. The linear relationship between the pop-in length and the load is not well respected in the presence of graphene (Fig. 6e). As shown in Figs. 6a and 6b, the presence of graphene affects the length of the pop-in as well as the onset of the first pop-in, revealing the influence of graphene on the nucleation and propagation of dislocations. The smaller pop-in length is the first evidence of the limitation of the number of dislocations participating in an avalanche in the presence of graphene. This effect of graphene has been revealed in recent literature (Chang et al., 2013; Wang et al., 2018; Zhang et al., 2019). Furthermore, the Cu<sub>A</sub>/Gr system never shows very large pop-ins when compared to the Cu<sub>A</sub> system, see Figs. 6f-i. The effect of graphene is the same in both nanoindentation modes while the less scattered distribution of pop-in lengths under displacement-control probably results from the lack of partly uncontrolled overshoot in this later mode.

AFM mappings of Cu<sub>A</sub> and Cu<sub>A</sub>/Gr systems after indentation confirm the effect of graphene by showing clear differences in the topography. In the Cu<sub>A</sub> system, the presence of a particle-like pattern (Gaillard et al., 2003) indicates the sustained activity of dislocations along the same slip planes leading to larger and sharper pile-ups around the indent, see Fig. 10c. In the presence of graphene, see Fig. 10d, there are no marked patterns around the indents, which would otherwise indicate that dislocations could escape by piercing through the surface. This leads to smoother pile-ups around the indent. The heights of the pile-ups have been measured for both Cu<sub>A</sub> and Cu<sub>A</sub>/Gr systems based on sections across several indents. Figs. 10g-h show height profiles corresponding to three sections on the indents shown in Figs. 10e-f which quantitatively prove the effect of graphene on the height of the pile-ups. To make it clearer, one of the profiles

is shown separately in Figs. 10i-j for both systems. The average values of the pile-up height were measured for five different indents on both systems and are equal to 26 nm for Cu<sub>A</sub> and 3 nm for Cu<sub>A</sub>/Gr, respectively.

The TEM observations confirm, from another angle, the interpretation above. The micrograph in Fig. 11a reveals a relatively localized mode of plastic deformation under the indent for Cu<sub>A</sub> along specific slip planes, as predicted by the DDD simulations as well. The high density of dislocations walls near the edges of the indented region is proof of the formation of pile-ups around the indents. Even though the AFM and TEM data are obtained from indents significantly deeper than the penetration corresponding to the first pop-ins, they represent the aggregated effect associated with the accumulation of several pop-ins and plastic activity. They concur to the same message: the dislocations mobilized to accommodate the penetration of the indent are more homogeneously distributed under the indented region showing that other slip systems must be activated in the presence of a graphene barrier (Fig. 11b).

The DDD simulations provide quantitative explanations for these observations. The simulations show that the dislocation arrangement is completely different when comparing Cu<sub>A</sub> with and without graphene coating (see Figure 15). For the Cu<sub>A</sub> system, the plastic zone exhibits a spherical shape while for Cu<sub>A</sub>/Gr, the plastic volume resembles a large half-sphere. The load very much increases in Cu<sub>A</sub>/Gr after the first plastic burst, which shows that an alternative mechanism of deformation starts at this point. Generally speaking, dislocation accumulated at an interface could lead to both directional back stress hardening and non-directional accumulation of obstacles which alleviate further dislocation motion that results in isotropic hardening (Fribourg et al., 2011; Zhao et al., 2019). A detailed analysis of the internal stress field induced by the dislocations indicates that the stress component normal to the free surface has a much longer range in the Cu<sub>A</sub>/Gr system compared to Cu<sub>A</sub>. This can be appreciated when comparing the evolution of the internal stress at different indentation depths in Fig 16 (up) Cu<sub>A</sub>

and (down) Cu<sub>A</sub>/Gr. Therefore, large back stress builds up in the system with graphene, which forces the dislocations to glide on other slip planes, hence delocalizing the plastic activity and leading to larger plastic volume, which can be clearly seen at the indentation depth of 60 nm in Fig. 16 (down). In the sample with no graphene, dislocations are not arrested and can move freely towards the surface. There is only a very small back stress generation at 60 nm penetration depth, see Fig. 16 (up). All these results from indentation, TEM, AFM and DDD simulations confirm the ability of graphene to block the transmission of dislocations between layers but also to delocalize the dislocation activity.

Nevertheless, the DDD simulations overestimate the load increase after the pop-in has occurred. This suggests that an additional mechanism takes place in Cu<sub>A</sub>/Gr, limiting the force increase. The discrepancy most probably comes from the partial debonding, fracture, and/or slipping observed at the Cu/Gr interface, which is not taken into account in the DDD simulations. Preliminary simulations with a stress-based adhesion criterion show indeed that debonding reduces the load after the pop-in compared to perfect adhesion. Upon debonding, dislocations are free to move out of the material and relax the load compared to an impenetrable boundary. Further works aim at addressing this question of the impact of a limited adhesion of graphene on the plasticity mechanisms.

Another observation induced by the presence of graphene is its influence on the onset of plasticity. This is probably the most unexpected result in this study. The presence of graphene causes the plasticity to start sooner when compared to the Cu<sub>A</sub> system. Elementary linear elastic finite element simulations of a system made of a stiff coating such as graphene lying on a more compliant substrate (with a factor 10 stiffness mismatch) have been performed with the software Abaqus. We only found an extremely small increase of the maximum shear stress or of the equivalent von Mises below the indent at penetration deeper than a few nanometers, hardly explaining why plasticity could start much sooner in the presence of graphene. The

second explanation for the earlier onset of plasticity could find its origin in the small roughness generated at the Cu surface in the presence of graphene (Fig. 10b). These perturbations could create stress concentrations that would trigger earlier pop-ins. Nevertheless, the length scale associated with this roughness is on the order of a micrometer. The first pop-in usually occurs at indentation depth typically below 20 nm. The contact region is thus smaller than 100 nm, which is one order of magnitude smaller. Hence, the argument is not convincing either. Finally, the best explanation comes from the indirect stiffening effect induced by the adhesionless contact in the presence of graphene, as evidenced by MD simulations, and explained at the beginning of the discussion. This means that, in the  $\text{Cu}_A/\text{Gr}$  system, a higher load is required for the same indentation depth, as seen in Fig 6a, for very small indentation depth ( $< 10$  nm). A higher load leads to larger stress levels under the indent, which causes an earlier onset of plasticity in the presence of graphene.

#### *4.2 Other systems*

The purpose of the investigation performed on the  $\text{Cu}_A/\text{Cu}_N$  and  $\text{Cu}_A/\text{Gr}/\text{Cu}_N$  systems was to shed light upon the application of graphene for reinforcing metallic systems through a composite effect associated with the insertion of hard interfaces. In this system, the graphene layer is sandwiched between two copper films having two very different grain sizes. The nanoindentation response is obviously sensitive to the specific properties of the two layers, independently of the presence or not of graphene. But, while the cap layer is the same in both  $\text{Cu}_A/\text{Cu}_N$  and  $\text{Cu}_A/\text{Gr}/\text{Cu}_N$  systems, any differences in the behaviour between these two systems can be attributed to the presence of the graphene layer.

The smaller pop-in length in the case of  $\text{Cu}_A/\text{Gr}/\text{Cu}_N$  compared to  $\text{Cu}_A/\text{Cu}_N$  shown in Figs. 7a and 7b reveals again the effect of graphene on dislocation glide. The comparison of the TEM micrographs for the two systems demonstrates that graphene blocks the movement of the mobile dislocations in the  $\text{Cu}_A$  substrate towards the surface, which results in large back stress

(Figs. 12a-b). Furthermore, a higher load is required to produce the same pop-in length (hence, the same number of dislocations involved in the avalanche) in  $\text{Cu}_A/\text{Gr}/\text{Cu}_N$  as graphene makes the glide of dislocations more difficult (Figure 12c). From a methodological viewpoint, this sandwich structure is the most elementary stack that can be imagined to test the bulk strengthening effect of graphene. Deconvoluting the effect of graphene from the indentation curve in order to predict an expected change of yield stress for instance is not straightforward and left for future works. But, the present results show that the approach is very sensitive to the presence of graphene and can be used to easily compare different configurations, graphene qualities, number of stacks without producing a bulk system.

There are two more findings not related to the presence of graphene but worth discussing further. The focus on the load-displacement curve of  $\text{Cu}_A/\text{Cu}_N$  in Fig. 8 shows several very small pop-ins before the main large pop-in in the  $\text{Cu}_A/\text{Cu}_N$  system which is connected with the high density of grain boundaries in the nanocrystalline copper. The high density of grain boundaries hinders the activity of dislocations and causes only small burst of dislocations instead of a true avalanche. The limited burst leads to the formation of only very small pop-ins during indentation (Kim et al., 2013; Rupert et al., 2012) which explains also the different behaviour in terms of hardness evolution at small indentation depth in Fig. 9. After the elastic regime below 10 nm indentation depth, the hardness of the  $\text{Cu}_N$  is found to be  $\sim 2.5$  GPa. The hardness of  $\text{Cu}_N$  moderately increases, probably due to the interaction of the plastic flow with the constrained interface with  $\text{Cu}_A$ . Further increase of the penetration leads to the burst of plasticity inside the  $\text{Cu}_A$  underneath layer, associated with a large pop-in. The hardness then converges towards the hardness  $\text{Cu}_A$ , near 1.4 GPa, with a slight, but continuous decrease with penetration associated with the indentation size effect. Assuming a ratio of 3 between the yield stress and hardness, the yield stress of  $\text{Cu}_N$  would be  $\sim 800$ MPa. This value is in the expected range for 50-100 nm grain size using the Hall-Petch law parameters as established for instance

in the literature (Cheng et al., 2005; Lu et al., 2010). The yield stress of the  $\text{Cu}_A$  film is more difficult to determine (Gertsman et al., 1994) as the response corresponds to a single crystal (for which the parameter “3” does not apply due to strain hardening and strain gradient plasticity effects) with no interaction with the grain boundaries nor with the Si substrate for the investigated range of indentation depth which remains smaller than 1/10 of the film thickness. The important conclusion is that the strength of  $\text{Cu}_N$  is much larger than for  $\text{Cu}_A$  at least by a factor of two. Furthermore, once the plasticity has started in  $\text{Cu}_A$ , the presence of the  $\text{Cu}_N$  cap layer does not play a major role anymore in dictating the overall hardness of the system, which is similar to a bare  $\text{Cu}_A$  layer.

The other finding when comparing the  $\text{Cu}_A$  and  $\text{Cu}_A/\text{Cu}_N$  systems is the length of the first pop-in which is much larger in the  $\text{Cu}_A/\text{Cu}_N$  system. The first large pop-in occurs at higher load and higher penetration in the  $\text{Cu}_A/\text{Cu}_N$  system leading to the activation of more dislocation sources during the indentation process (Fig. 8). There can be three different sources of dislocations including; pre-existing dislocations, punched-out dislocations during deformation, and threading dislocations [17,42]. In the case of annealed copper, the first displacement burst results from the full avalanche of the pre-existing dislocations and punched-out dislocations during nanoindentation when the local energy underneath and around the indenter reaches a critical value. In the case of the  $\text{Cu}_A/\text{Cu}_N$  systems, the small grain size in the nanocrystalline  $\text{Cu}_N$  cap layer prevents the development of significant avalanche of dislocations immediately blocked by the high density of grain boundaries, confirmed also by the smooth evolution of hardness in Fig. 9. Very large elastic energy builds up under the indent inside the cap layer until the threshold for initiating plasticity in the  $\text{Cu}_A$  is attained. This large amount of elastic energy is released through very large pop-ins. In other words, the presence of the cap layer can be simply seen as a way to avoid any pop-in in the  $\text{Cu}_A$  substrate before a large load is attained.

## 5. Conclusion

The plastic deformation behaviour of copper upon nanoindentation has been studied for two different configurations involving a single graphene layer. The main findings of the work are the following :

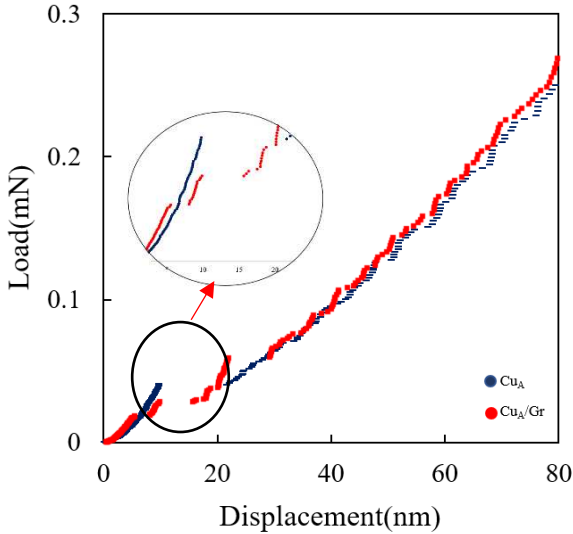
- The pop-in length is, on average, shorter in the presence of a graphene layer, as confirmed under both force- and displacement-controlled indentation modes. As a side conclusion, we prove that the results obtained by both modes agree with one another regarding pop-in behaviour.
- TEM analysis of cross-sections taken below the indents shows that the dislocation activity occurs in a much larger volume and is more homogenous in the presence of graphene. This is associated with a much smoother pop-in and the absence of slip steps on the surface, as measured by AFM.
- 3D DDD simulations reveal that the origin of these effects is the large back stress induced by the presence of the impenetrable graphene barrier, leading to the spreading and delocalization of the plasticity process.
- Plasticity starts earlier in the presence of graphene compared to bare Cu, presumably due to higher stress levels associated with adhesionless contact, compared to bare Cu.
- Another side result of this study is the interest to look at an elementary stack made of a graphene layer intercalated under a cap layer to quantify its potential impact on the strength when inserted in the bulk of materials.

In conclusion, the presence of a single layer of graphene as a coating or interlayer below a Cu cap layer modifies the plastic flow under the contact for indentation depth much larger than the graphene layer thickness, by spreading the plasticity over a much larger volume. The impact is mainly on the pop-in behaviour and smoothing of the pile-ups. This delocalization of the plasticity can be useful for applications involving repeated contacts to mitigate the induced

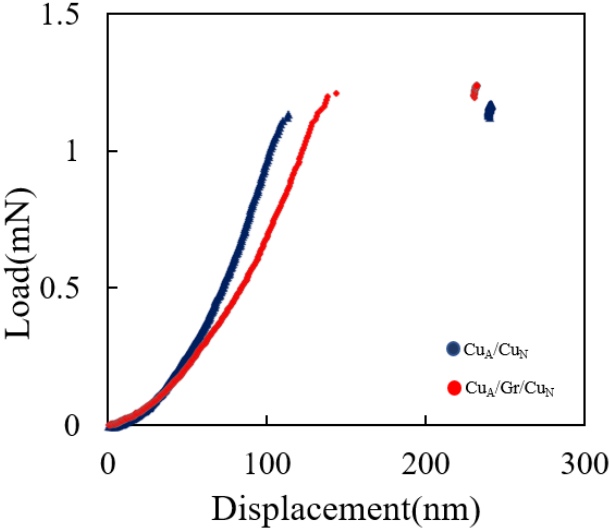


roughness such as in electrical switches or under mild erosion conditions where the amplitude of the induced roughness under impact is often responsible for the wear mechanism. Nevertheless, the magnitude of the effects discussed in the work is not large enough to provide significant wear or erosion mitigation with a single graphene layer in the case of severe loading conditions.

**Appendix.** Examples of raw data load-displacement curves:



(a)



(b)

**Figure A1** (a) Comparison of representative force-penetration curves for  $Cu_A$  and  $Cu_A/Gr$ ; (a) Comparison of representative force-penetration curves for  $Cu_A/Cu_N$  and  $Cu_A/Gr/Cu_N$ .

## **Acknowledgments**

This work was supported by the ARC project Naturist Convention No11/16-037 and by the FNRS under Grant PDR – T.0178.19. B.H. was also supported by the WBI world excellence fellowship for one year at Penn State University. The authors are thankful to S. Ryelandt for her support during the nanoindentation process and M.W. Malik for his advice for CVD-graphene growth. H.I. is mandated by the Belgian National Fund for Scientific Research (FSR-FNRS).

## References

- Bartolucci, S.F., Paras, J., Rafiee, M.A., Rafiee, J., Lee, S., Kapoor, D., Koratkar, N., 2011. Graphene-aluminum nanocomposites. *Mater. Sci. Eng. A* 528, 7933–7937. <https://doi.org/10.1016/j.msea.2011.07.043>
- Britton, T.B., Liang, H., Dunne, F.P.E., Wilkinson, A.J., 2010. The effect of crystal orientation on the indentation response of commercially pure titanium: Experiments and simulations. *Proc. R. Soc. A Math. Phys. Eng. Sci.* 466, 695–719. <https://doi.org/10.1098/rspa.2009.0455>
- Chang, H.J., Fivel, M., Rodney, D., Verdier, M., 2010. Simulations multi-échelles de l'indentation de métaux CFC: De l'atome au milieu continu. *Comptes Rendus Phys.* 11, 285–292. <https://doi.org/10.1016/j.crhy.2010.07.007>
- Chang, S.W., Nair, A.K., Buehler, M.J., 2013. Nanoindentation study of size effects in nickel-graphene nanocomposites. *Philos. Mag. Lett.* 93, 196–203. <https://doi.org/10.1080/09500839.2012.759293>
- Chen, L.Y., Konishi, H., Fehrenbacher, A., Ma, C., Xu, J.Q., Choi, H., Xu, H.F., Pfefferkorn, F.E., Li, X.C., 2012. Novel nanoprocessing route for bulk graphene nanoplatelets reinforced metal matrix nanocomposites. *Scr. Mater.* 67, 29–32. <https://doi.org/10.1016/j.scriptamat.2012.03.013>
- Cheng, S., Ma, E., Wang, Y.M., Kecskes, L.J., Youssef, K.M., Koch, C.C., Trociewitz, U.P., Han, K., 2005. Tensile properties of in situ consolidated nanocrystalline Cu. *Acta Mater.* 53, 1521–1533. <https://doi.org/10.1016/j.actamat.2004.12.005>
- Choi, W., Lahiri, I., Seelaboyina, R., Kang, Y.S., 2010. Synthesis of graphene and its applications: A review. *Crit. Rev. Solid State Mater. Sci.* 35, 52–71. <https://doi.org/10.1080/10408430903505036>
- Corcoran, S., Colton, R., Lilleodden, E., Gerberich, W., 1997. Anomalous plastic deformation at surfaces: Nanoindentation of gold single crystals. *Phys. Rev. B - Condens. Matter Mater. Phys.* 55, R16057–R16060. <https://doi.org/10.1103/PhysRevB.55.R16057>
- Dehm, G., Jaya, B.N., Raghavan, R., Kirchlechner, C., 2018. Overview on micro- and nanomechanical testing: New insights in interface plasticity and fracture at small length scales. *Acta Mater.* 142, 248–282. <https://doi.org/10.1016/j.actamat.2017.06.019>
- Dorri Moghadam, A., Omrani, E., Menezes, P.L., Rohatgi, P.K., 2015. Mechanical and tribological properties of self-lubricating metal matrix nanocomposites reinforced by carbon nanotubes (CNTs) and graphene - A review. *Compos. Part B Eng.* 77, 402–420. <https://doi.org/10.1016/j.compositesb.2015.03.014>

- Fivel, M., Depres, C., 2014. An easy implementation of displacement calculations in 3D discrete dislocation dynamics codes. *Philos. Mag.* 94, 3206–3214.  
<https://doi.org/10.1080/14786435.2014.949326>
- Fivel, M.C., 2008. Discrete dislocation dynamics: an important recent break-through in the modelling of dislocation collective behaviour. *Comptes Rendus Phys.* 9, 427–436.  
<https://doi.org/10.1016/j.crhy.2007.11.005>
- Fivel, M.C., Robertson, C.F., Canova, G.R., Boulanger, L., 1998. Three-dimensional modeling of indent-induced plastic zone at a mesoscale. *Acta Mater.* 46, 6183–6194.  
[https://doi.org/10.1016/S1359-6454\(98\)00278-X](https://doi.org/10.1016/S1359-6454(98)00278-X)
- Fribourg, G., Bréchet, Y., Deschamps, A., Simar, A., 2011. Microstructure-based modelling of isotropic and kinematic strain hardening in a precipitation-hardened aluminium alloy. *Acta Mater.* 59, 3621–3635. <https://doi.org/10.1016/j.actamat.2011.02.035>
- Gaillard, Y., Tromas, C., Woïrgard, J., 2003. Pop-in phenomenon in MgO and LiF: Observation of dislocation structures. *Philos. Mag. Lett.* 83, 553–561.  
<https://doi.org/10.1080/09500830310001594273>
- Gertsman, V.Y., Hoffmann, M., Gleiter, H., Birringer, R., 1994. The study of grain size dependence of yield stress of copper for a wide grain size range. *Acta Metall. Mater.* 42, 3539–3544. [https://doi.org/10.1016/0956-7151\(94\)90486-3](https://doi.org/10.1016/0956-7151(94)90486-3)
- Gouldstone, A., Koh, H.J., Zeng, K.Y., Giannakopoulos, A.E., Suresh, S., 2000. Discrete and continuous deformation during nanoindentation of thin films. *Acta Mater.* 48, 2277–2295. [https://doi.org/10.1016/S1359-6454\(00\)00009-4](https://doi.org/10.1016/S1359-6454(00)00009-4)
- Hammad, M., Adjizian, J.J., Sacré, C.H., Huet, B., Charlier, J.C., Raskin, J.P., Pardoën, T., 2017. Adhesionless and near-ideal contact behavior of graphene on Cu thin film. *Carbon N. Y.* 122, 446–450. <https://doi.org/10.1016/j.carbon.2017.06.037>
- Huet, B., Raskin, J.P., 2018a. Role of Cu foil in-situ annealing in controlling the size and thickness of CVD graphene domains. *Carbon N. Y.* 129, 270–280.  
<https://doi.org/10.1016/j.carbon.2017.12.043>
- Huet, B., Raskin, J.P., 2018b. Role of the Cu substrate in the growth of ultra-flat crack-free highly-crystalline single-layer graphene. *Nanoscale* 10, 21898–21909.  
<https://doi.org/10.1039/c8nr06817h>
- Huet, B., Raskin, J.P., 2017. Pressure-Controlled Chemical Vapor Deposition of Single-Layer Graphene with Millimeter-Size Domains on Thin Copper Film. *Chem. Mater.* 29, 3431–3440. <https://doi.org/10.1021/acs.chemmater.6b04928>
- Hwang, J., Yoon, T., Jin, S.H., Lee, J., Kim, T.S., Hong, S.H., Jeon, S., 2013. Enhanced

- mechanical properties of graphene/copper nanocomposites using a molecular-level mixing process. *Adv. Mater.* 25, 6724–6729. <https://doi.org/10.1002/adma.201302495>
- Jian, S.R., Juang, J.Y., Chen, N.C., Jang, J.S.C., Huang, J.C., Lai, Y.S., 2010. Nanoindentation-induced structural deformation in GaN/AlN multilayers. *Nanosci. Nanotechnol. Lett.* 2, 315–321. <https://doi.org/10.1166/nnl.2010.1100>
- Kang, J.H., Moon, J., Kim, D.J., Kim, Y., Jo, I., Jeon, C., Lee, J., Hong, B.H., 2016. Strain Relaxation of Graphene Layers by Cu Surface Roughening. *Nano Lett.* 16, 5993–5998. <https://doi.org/10.1021/acs.nanolett.6b01578>
- Kese, K., Li, Z.C., 2006. Semi-ellipse method for accounting for the pile-up contact area during nanoindentation with the Berkovich indenter. *Scr. Mater.* 55, 699–702. <https://doi.org/10.1016/j.scriptamat.2006.06.030>
- Kim, Y., Lee, J., Yeom, M.S., Shin, J.W., Kim, H., Cui, Y., Kysar, J.W., Hone, J., Jung, Y., Jeon, S., Han, S.M., 2013. Strengthening effect of single-atomic-layer graphene in metal-graphene nanolayered composites. *Nat. Commun.* 4, 1–7. <https://doi.org/10.1038/ncomms3114>
- Klemenz, A., Pastewka, L., Balakrishna, S.G., Caron, A., Bennewitz, R., Moseler, M., 2014. Atomic scale mechanisms of friction reduction and wear protection by graphene. *Nano Lett.* 14, 7145–7152. <https://doi.org/10.1021/nl5037403>
- Kuang, D., Xu, L., Liu, L., Hu, W., Wu, Y., 2013. Graphene-nickel composites. *Appl. Surf. Sci.* 273, 484–490. <https://doi.org/10.1016/j.apsusc.2013.02.066>
- Lahiri, I., Verma, V.P., Choi, W., 2011. An all-graphene based transparent and flexible field emission device. *Carbon N. Y.* 49, 1614–1619. <https://doi.org/10.1016/j.carbon.2010.12.044>
- Li, Zan, Fu, X., Guo, Q., Zhao, L., Fan, G., Li, Zhiqiang, Xiong, D.B., Su, Y., Zhang, D., 2018. Graphene quality dominated interface deformation behavior of graphene-metal composite: The defective is better. *Int. J. Plast.* 111, 253–265. <https://doi.org/10.1016/j.ijplas.2018.07.020>
- Liu, X.Y., Wang, F.C., Wang, W.Q., Wu, H.A., 2016. Interfacial strengthening and self-healing effect in graphene-copper nanolayered composites under shear deformation. *Carbon N. Y.* 107, 680–688. <https://doi.org/10.1016/j.carbon.2016.06.071>
- Lu, N., Suo, Z., Vlassak, J.J., 2010. The effect of film thickness on the failure strain of polymer-supported metal films. *Acta Mater.* 58, 1679–1687. <https://doi.org/10.1016/j.actamat.2009.11.010>
- Materials, S., 2019. ce d M us pt 0–22.

- Moharrami, N., Bull, S.J., 2014. A comparison of nanoindentation pile-up in bulk materials and thin films. *Thin Solid Films* 572, 189–199. <https://doi.org/10.1016/j.tsf.2014.06.060>
- Ni, Z.H., Yu, T., Lu, Y.H., Wang, Y.Y., Feng, Y.P., Shen, Z.X., 2008. Uniaxial strain on graphene: Raman spectroscopy study and band-gap opening. *ACS Nano* 2, 2301–2305. <https://doi.org/10.1021/nn800459e>
- Nieto, A., Bisht, A., Lahiri, D., Zhang, C., Agarwal, A., 2017. Graphene reinforced metal and ceramic matrix composites: a review. *Int. Mater. Rev.* 62, 241–302. <https://doi.org/10.1080/09506608.2016.1219481>
- Oliver, W.C., Pharr, G.M., 1992. An improved technique for determining hardness and elastic modulus using load and displacement. *J Mater Res* 7, 1564–1583.
- Ovid'ko, I.A., 2013. Mechanical properties of graphene. *Rev. Adv. Mater. Sci.* <https://doi.org/10.1039/c2nr31164j>
- Park, S.Y., Gwak, E.J., Huang, M., Ruoff, R.S., Kim, J.Y., 2017. Nanolaminate of metallic glass and graphene with enhanced elastic modulus, strength, and ductility in tension. *Scr. Mater.* 139, 63–66. <https://doi.org/10.1016/j.scriptamat.2017.06.031>
- Park, S.Y., Kim, Y.C., Ruoff, R.S., Kim, J.Y., 2019. Incipient plasticity and fully plastic contact behavior of copper coated with a graphene layer. *APL Mater.* 7. <https://doi.org/10.1063/1.5086333>
- Pharr, G.M., Oliver, W.C., 1992. Measurement of Thin Film Mechanical Properties Using Nanoindentation. *MRS Bull.* 17, 28–33. <https://doi.org/10.1557/S0883769400041634>
- Porwal, H., Grasso, S., Reece, M.J., 2013. Review of graphene-ceramic matrix composites. *Adv. Appl. Ceram.* 112, 443–454. <https://doi.org/10.1179/174367613X13764308970581>
- Rupert, T.J., Trelewicz, J.R., Schuh, C.A., 2012. Grain boundary relaxation strengthening of nanocrystalline Ni-W alloys. *J. Mater. Res.* 27, 1285–1294. <https://doi.org/10.1557/jmr.2012.55>
- Sato, Y., Shinzato, S., Ohmura, T., Ogata, S., 2019. Atomistic prediction of the temperature- And loading-rate-dependent first pop-in load in nanoindentation. *Int. J. Plast.* 121, 280–292. <https://doi.org/10.1016/j.ijplas.2019.06.012>
- Selvarajou, B., Shin, J.H., Ha, T.K., Choi, I.S., Joshi, S.P., Han, H.N., 2014. Orientation-dependent indentation response of magnesium single crystals: Modeling and experiments. *Acta Mater.* 81, 358–376. <https://doi.org/10.1016/j.actamat.2014.08.042>
- Shibutani, Y., Tsuru, T., Koyama, A., 2007. Nanoplastic deformation of nanoindentation: Crystallographic dependence of displacement bursts. *Acta Mater.* 55, 1813–1822. <https://doi.org/10.1016/j.actamat.2006.10.055>

- Suresh, S., Nieh, T.G., Choi, B.W., 1999. Nano-indentation of copper thin films on silicon substrates. *Scr. Mater.* 41, 951–957. [https://doi.org/10.1016/S1359-6462\(99\)00245-6](https://doi.org/10.1016/S1359-6462(99)00245-6)
- Tjong, S.C., 2013. Recent progress in the development and properties of novel metal matrix nanocomposites reinforced with carbon nanotubes and graphene nanosheets. *Mater. Sci. Eng. R Reports* 74, 281–350. <https://doi.org/10.1016/j.mser.2013.08.001>
- Verdier, M., Fivel, M., Groma, I., 1998. Mesoscopic scale simulation of dislocation dynamics in fcc metals: Principles and applications. *Model. Simul. Mater. Sci. Eng.* 6, 755–770. <https://doi.org/10.1088/0965-0393/6/6/007>
- Wang, L., Jin, J., Cao, J., Yang, P., Peng, Q., 2018. Interaction of edge dislocations with graphene nanosheets in graphene/Fe composites. *Crystals* 8, 1–10. <https://doi.org/10.3390/cryst8040160>
- Yi, D., Luo, D., Wang, Z.J., Dong, J., Zhang, X., Willinger, M.G., Ruoff, R.S., Ding, F., 2018. What Drives Metal-Surface Step Bunching in Graphene Chemical Vapor Deposition? *Phys. Rev. Lett.* 120, 246101. <https://doi.org/10.1103/PhysRevLett.120.246101>
- Zhang, C., Lu, C., Pei, L., Li, J., Wang, R., Tieu, K., 2019. The negative Poisson's ratio and strengthening mechanism of nanolayered graphene/Cu composites. *Carbon N. Y.* 143, 125–137. <https://doi.org/10.1016/j.carbon.2018.10.097>
- Zhao, L., Guo, Q., Li, Z., Xiong, D.B., Osovski, S., Su, Y., Zhang, D., 2019. Strengthening and deformation mechanisms in nanolaminated graphene-Al composite micro-pillars affected by graphene in-plane sizes. *Int. J. Plast.* 116, 265–279. <https://doi.org/10.1016/j.ijplas.2019.01.006>
- Zhu, X., Zhao, Y., Ma, L., Zhang, G., Ren, W., Peng, X., Hu, N., Rintoul, L., Bell, J.M., Yan, C., 2019. Graphene coating makes copper more resistant to plastic deformation. *Compos. Commun.* 12, 106–111. <https://doi.org/10.1016/j.coco.2019.01.006>

**Figure 1.** Schematics of the four different investigated systems; (a) annealed Cu film 1200 nm-thick ( $\text{Cu}_A$ ); (b) graphene as grown on a 1200 nm-thick Cu film ( $\text{Cu}_A/\text{Gr}$ ); (c) 100 nm-thick nanocrystalline Cu film evaporated on a 1200 nm-thick annealed Cu film ( $\text{Cu}_A/\text{Cu}_N$ ); (d) 100 nm-thick nanocrystalline Cu film evaporated on as-grown graphene ( $\text{Cu}_A/\text{Gr}/\text{Cu}_N$ ).

**Figure 2.** Geometry of the dislocation nucleation process under the indent within the 3D DDD framework, consisting of 3 interstitial prismatic loops as determined from MD simulations in the case of (111) spherical indentation.

**Figure 3.** Typical Raman spectrum directly acquired on as-grown graphene. D, G, and 2D – band, respectively located at 1350, 1580 and 2690  $\text{cm}^{-1}$  are the main Raman peaks expected for graphene.

**Figure 4.** Grain characteristics of the Cu films; SEM micrographs of (a) the 1200 nm thick  $\text{Cu}_A$  film; (b) 100 nm thick  $\text{Cu}_N$  film; (c) EBSD map; (d) pole figures.

**Figure 5.** SEM micrograph showing a series of indent inside a  $\text{Cu}_A$  grain, sufficiently remote from grain boundaries to avoid plastic interactions.

**Figure 6.** (a) Comparison of load-penetration curves for  $\text{Cu}_A$  and  $\text{Cu}_A/\text{Gr}$  in load-control mode; (b) comparison of load-penetration curves for  $\text{Cu}_A$  and  $\text{Cu}_A/\text{Gr}$  in displacement-control mode; (c) first and second pop-ins in  $\text{Cu}_A$  system; (d) first, second, and third pop-ins in  $\text{Cu}_A/\text{Gr}$  system; (e) comparison the length of first and second pop-ins of  $\text{Cu}_A$  with first, second and third pop-ins of  $\text{Cu}_A/\text{Gr}$  in load-control mode; (f) comparison the first pop-in length vs load of  $\text{Cu}_A$  and  $\text{Cu}_A/\text{Gr}$  in load-control mode; (g) comparison the first pop-in length vs load of  $\text{Cu}_A$  and  $\text{Cu}_A/\text{Gr}$  in displacement-control mode; (h) comparison of probability function vs load of  $\text{Cu}_A$  and  $\text{Cu}_A/\text{Gr}$  in load-control mode; (i) comparison of probability function vs load of  $\text{Cu}_A$  and  $\text{Cu}_A/\text{Gr}$  in displacement-control mode.

**Figure 7.** (a) Comparison of the load-penetration curves for  $\text{Cu}_A/\text{Cu}_N$  and  $\text{Cu}_A/\text{Gr}/\text{Cu}_N$  in load-control mode; (b) comparison of the first pop-in length of  $\text{Cu}_A/\text{Cu}_N$  and  $\text{Cu}_A/\text{Gr}/\text{Cu}_N$  in load-control mode.

**Figure 8.** Comparison of pop-in length for  $\text{Cu}_A$  and  $\text{Cu}_A/\text{Cu}_N$ . The inset shows the small pop-ins in one of the curves which occur before the first large pop-in in  $\text{Cu}_A/\text{Cu}_N$ .

**Figure 9.** Variation of hardness as a function of penetration depth for  $\text{Cu}_A$  and  $\text{Cu}_A/\text{Cu}_N$ , showing the significantly larger hardness of before  $\text{Cu}_N$  before the plasticity is transferred into the underlying  $\text{Cu}_A$  layer with the hardness following then the trend obtained for a single  $\text{Cu}_A$  film.

**Figure 10.** (a) AFM image before indentation on  $\text{Cu}_A$  (size of the square box is 44.5 x 44.5  $\mu\text{m}^2$ ); (b) AFM image before indentation on  $\text{Cu}_A/\text{Gr}$  (size of the square box is 44.5 x 44.5  $\mu\text{m}^2$ ); (c) AFM image after indentation on  $\text{Cu}_A$  (size of the square box is 25 x 25  $\mu\text{m}^2$ ); (d) AFM



image after indentation on Cu<sub>A</sub>/Gr (size of the square box is 25 x 25 μm<sup>2</sup>); (e) Higher magnification of one indent on Cu<sub>A</sub>; (f) higher magnification on one indent on Cu<sub>A</sub>/Gr; Cu<sub>A</sub>; (g) three height profiles across the indent shown in (e); (h) three height profiles across the indent shown in (f); (i) height profile (dark blue) across the indent shown in (e); (j) height profile (red) across the indent shown in (f).

**Figure 11.** (a) TEM micrograph showing the dislocation arrangements in Cu<sub>A</sub>; (b) TEM micrograph showing the dislocations structures in the Cu<sub>A</sub>/Gr system. The two top layers consist of successively deposited electron beam Pt layer and ion beam Pt layer from the left to the right side, respectively.

**Figure 12.** (a) TEM micrograph showing the dislocation structure under a 100 nm-deep indent in the Cu<sub>A</sub>/Cu<sub>N</sub> film; (b) TEM micrograph showing the dislocation structure under a 100 nm-deep indent in the Cu<sub>A</sub>/Gr/Cu<sub>N</sub> film; (c) comparison of the load-penetration curves for Cu<sub>A</sub>/Cu<sub>N</sub> and Cu<sub>A</sub>/Gr/Cu<sub>N</sub> under load-control mode.

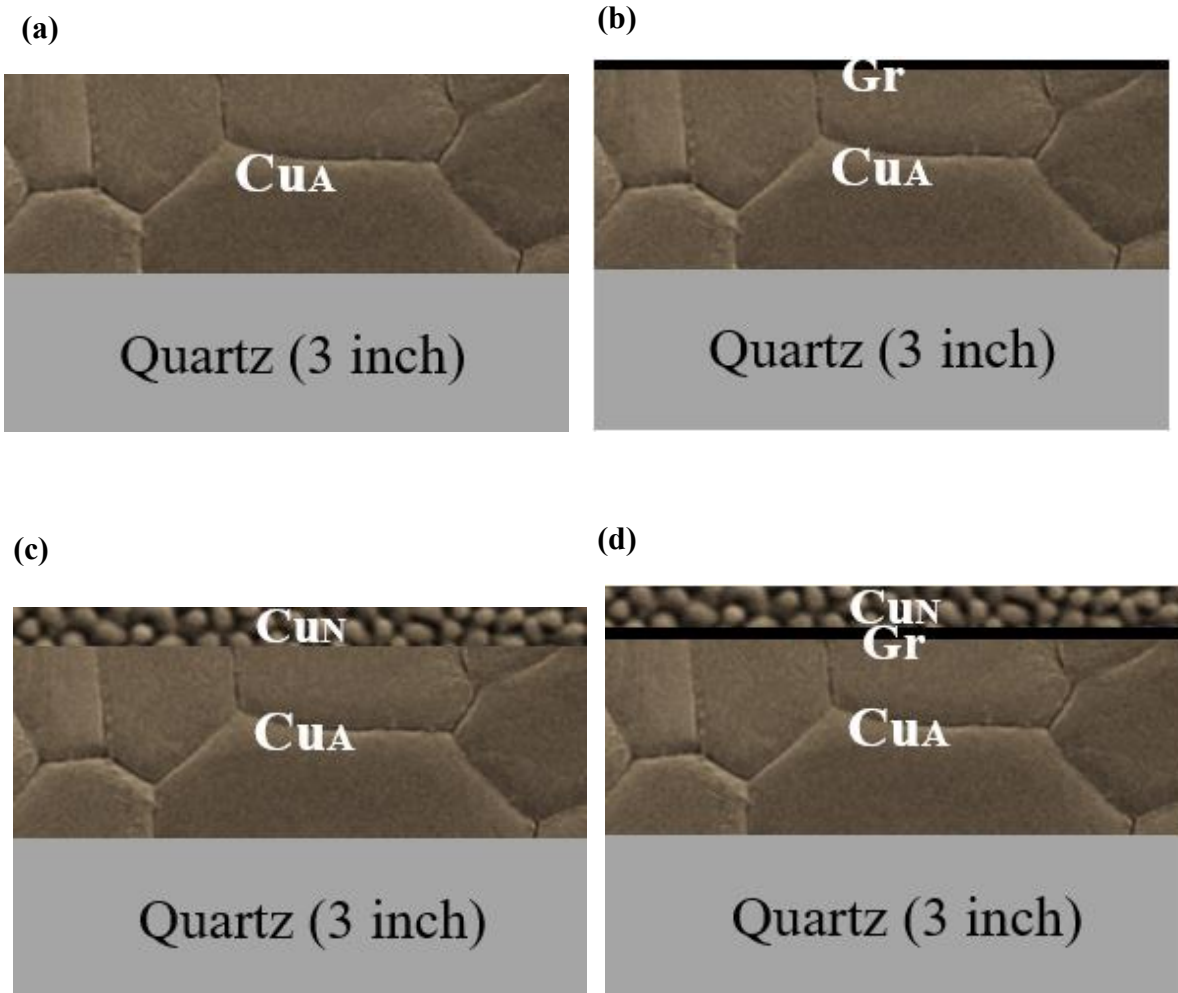
**Figure 13.** HAADF STEM micrograph of the region below an indent performed in a Cu<sub>A</sub>/Gr/Cu<sub>N</sub> system exhibiting decohesion/failure at the graphene layer level.

**Figure 14.** (a) DDD predicted load-penetration curve for Cu<sub>A</sub> for the different onset of the nucleation algorithm; (b) DDD load-penetration curve for Cu<sub>A</sub>/Gr, which shows a stiffer mechanical response.

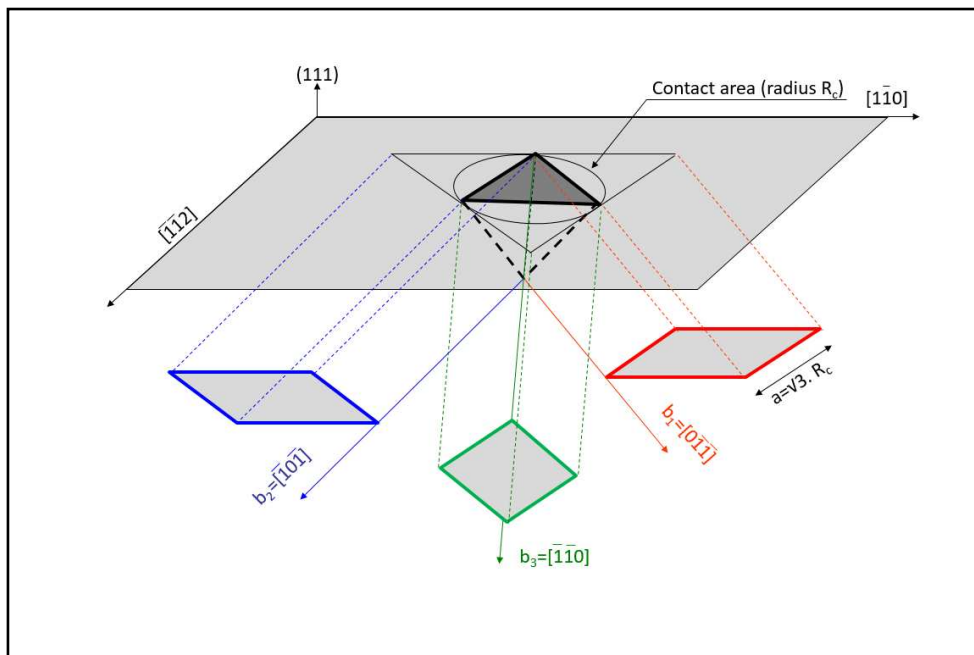
**Figure 15.** (a) DDD load-penetration curve and evolution of dislocation density (filled circles) for Cu<sub>A</sub> and Cu<sub>A</sub>/Gr when plasticity is triggered at 10 nm depth; (b) dislocation arrangements for Cu<sub>A</sub> and Cu<sub>A</sub>/Gr at different instants of indentation as indicated on the load-penetration curve.

**Figure 16.** Evolution of the normal stress  $n^T \cdot \sigma \cdot n$  with  $n=(111)$  for different indentation depths inside (up) Cu<sub>A</sub>, (down) Cu<sub>A</sub>/Gr; the color range is within [-500MPa:500MPa]. Note a higher long-range normal stress zone in Cu<sub>A</sub>/Gr.

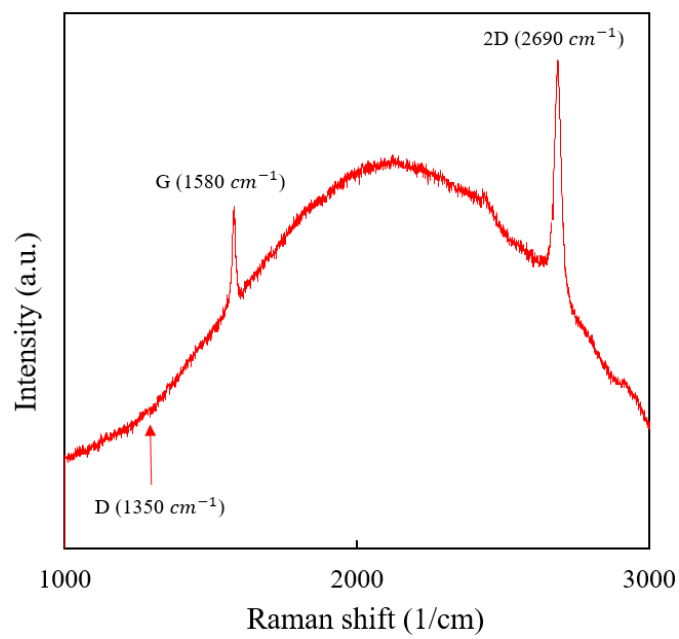
**Figure A1.** (a) Comparison of representative force-penetration curves for Cu<sub>A</sub> and Cu<sub>A</sub>/Gr; (a) Comparison of representative force-penetration curves for Cu<sub>A</sub>/Cu<sub>N</sub> and Cu<sub>A</sub>/Gr/Cu<sub>N</sub>.



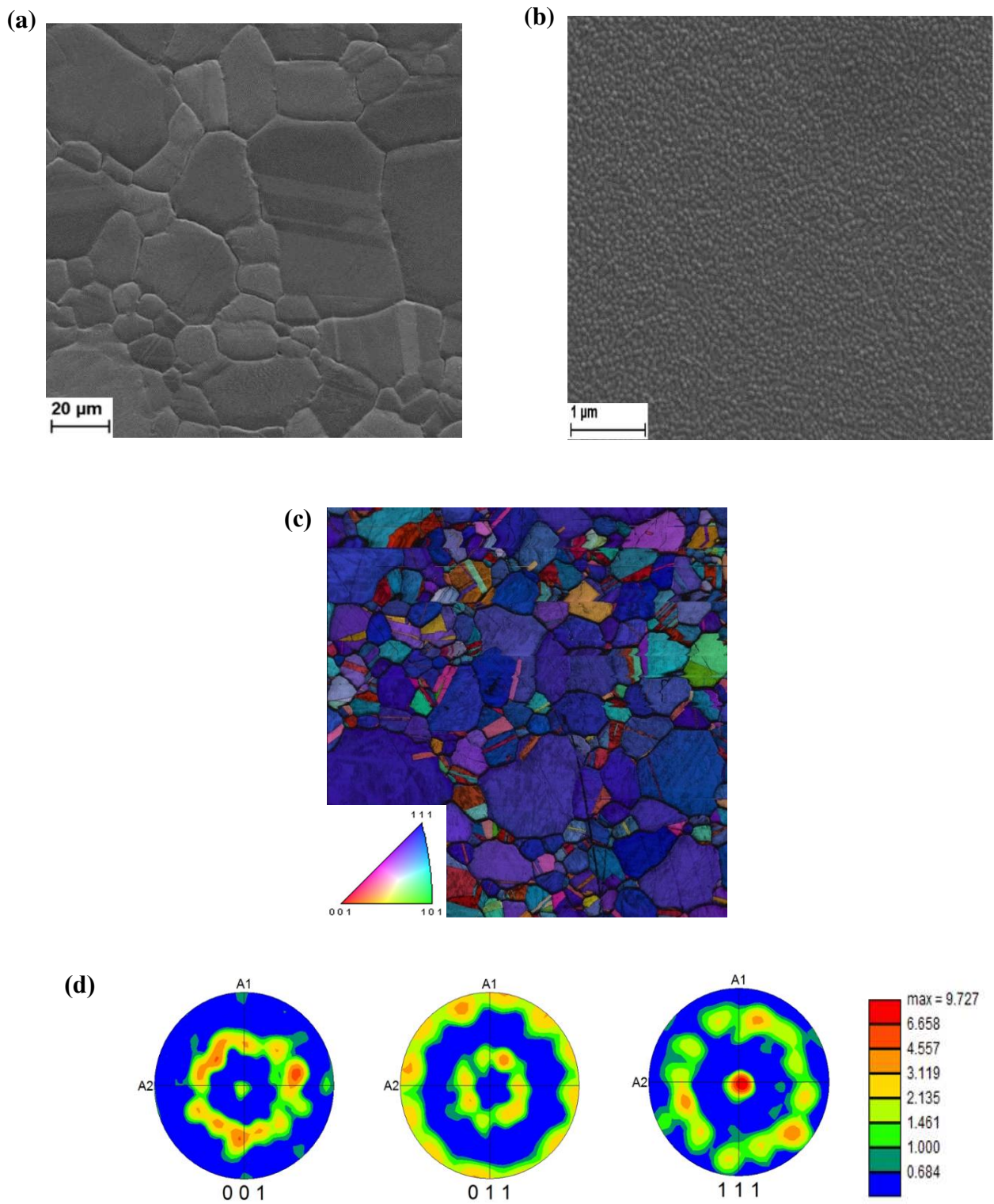
**Fig. 1.** Schematics of the four different investigated systems; (a) annealed Cu film 1200 nm-thick ( $\text{Cu}_A$ ); (b) graphene as grown on a 1200 nm-thick Cu film ( $\text{Cu}_A/\text{Gr}$ ); (c) 100 nm-thick nanocrystalline Cu film evaporated on a 1200 nm-thick annealed Cu film ( $\text{Cu}_A/\text{Cu}_N$ ); (d) 100 nm-thick nanocrystalline Cu film evaporated on as-grown graphene ( $\text{Cu}_A/\text{Gr}/\text{Cu}_N$ ).



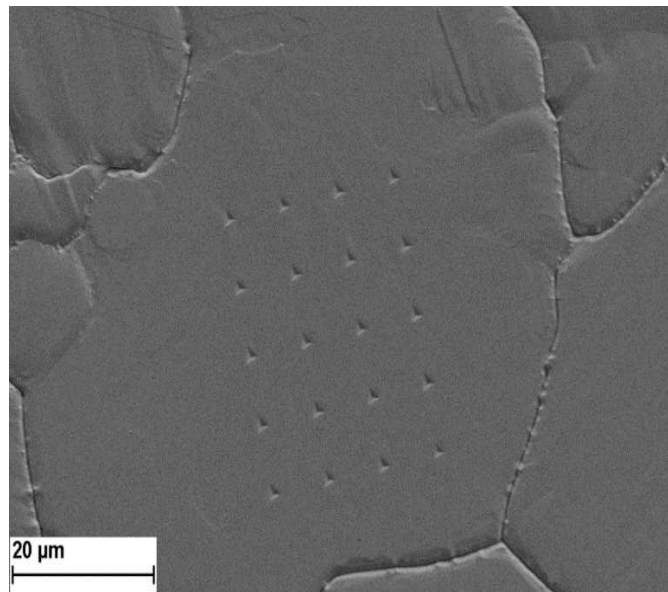
**Fig. 2.** Geometry of the dislocation nucleation process under the indent within the 3D DDD framework, consisting of 3 interstitial prismatic loops as determined from MD simulations in the case of (111) spherical indentation.



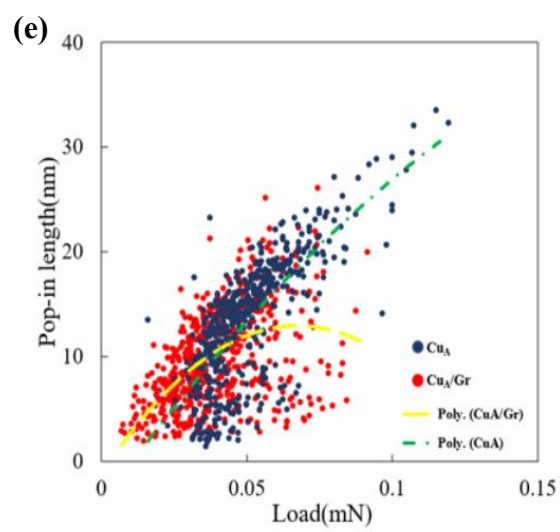
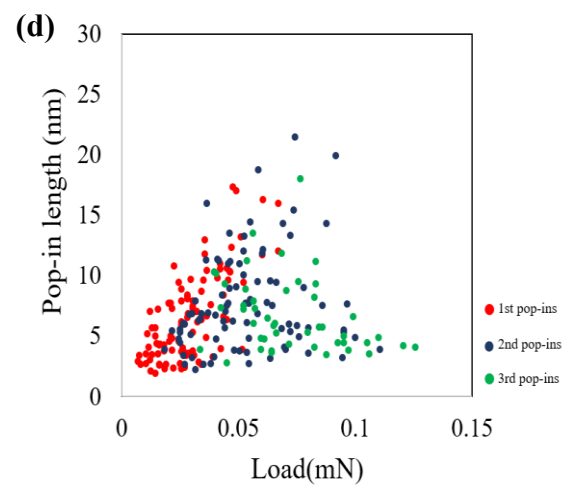
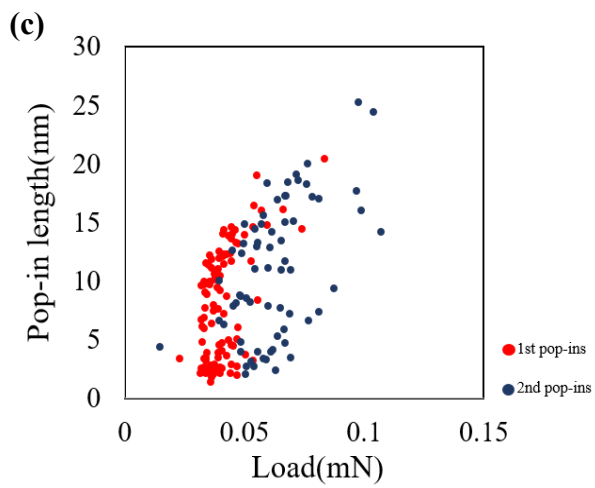
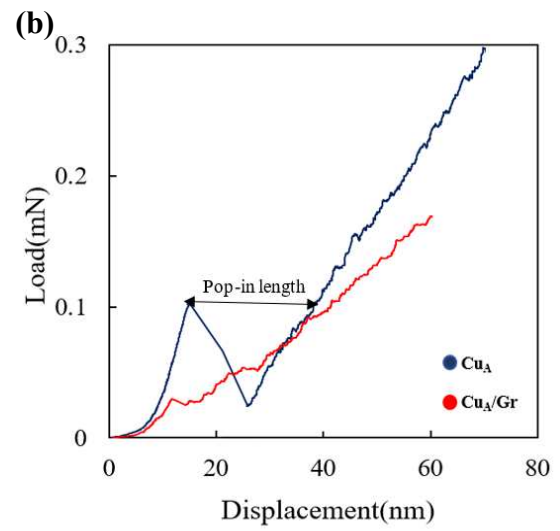
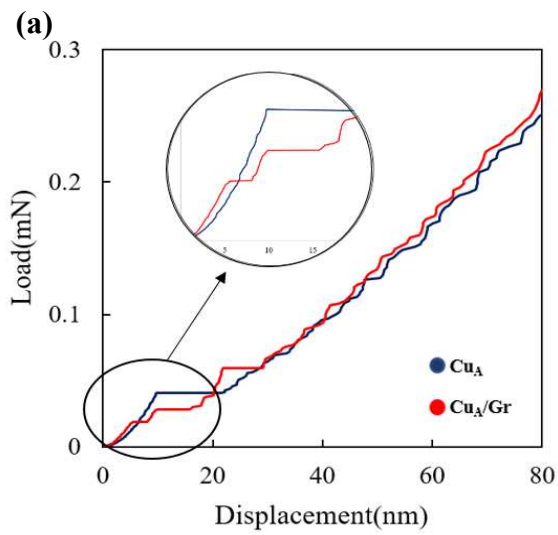
**Fig. 3.** Typical Raman spectrum directly acquired on as-grown graphene. D, G, and 2D –band, respectively located at 1350, 1580 and 2690  $\text{cm}^{-1}$ , are the main Raman peaks expected for graphene.

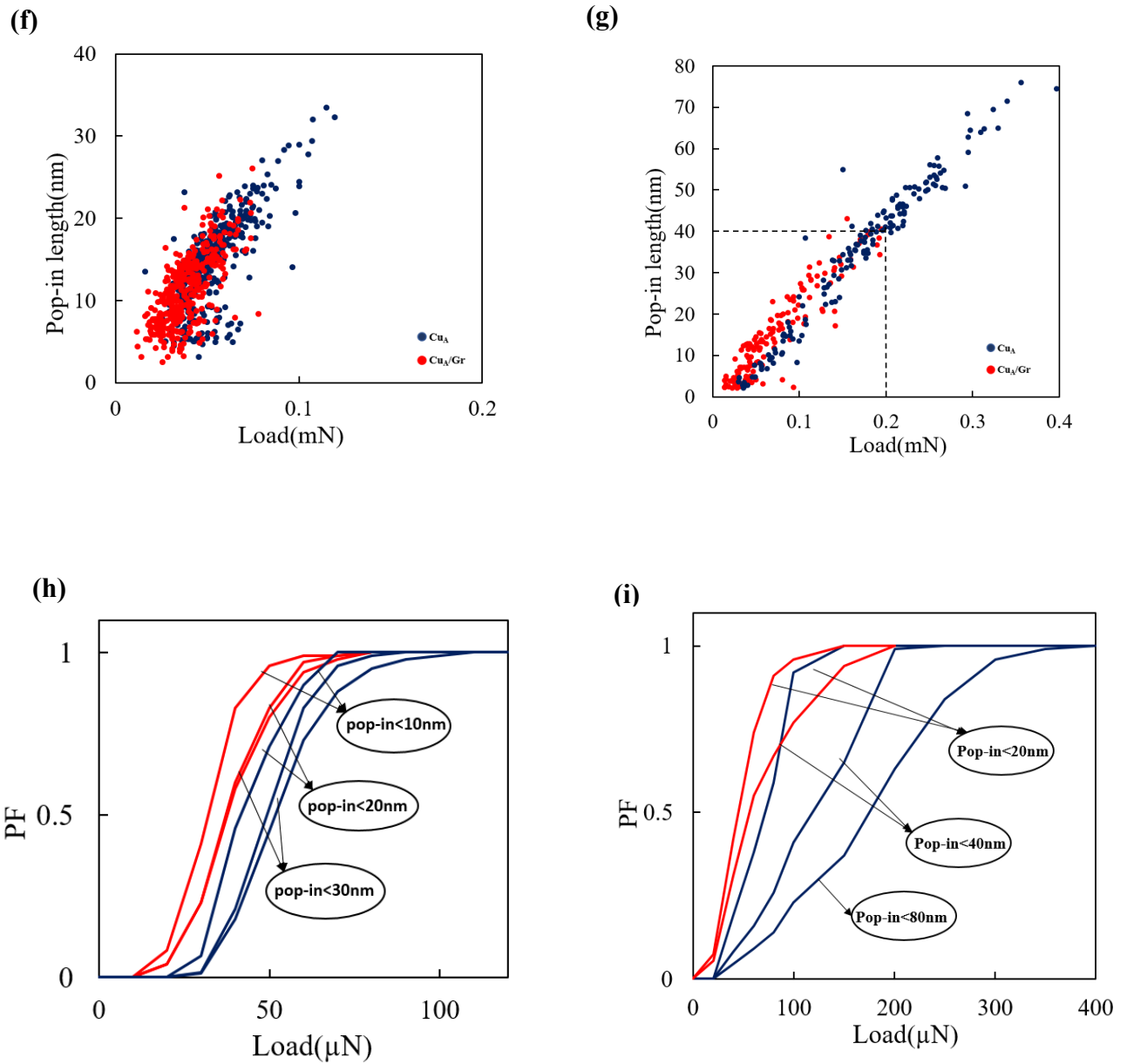


**Fig. 4.** Grain characteristics of the Cu films; SEM micrographs of (a) the 1200 nm thick  $\text{Cu}_A$  film; (b) 100 nm thick  $\text{Cu}_N$  film; (c) EBSD map; (d) pole figures.



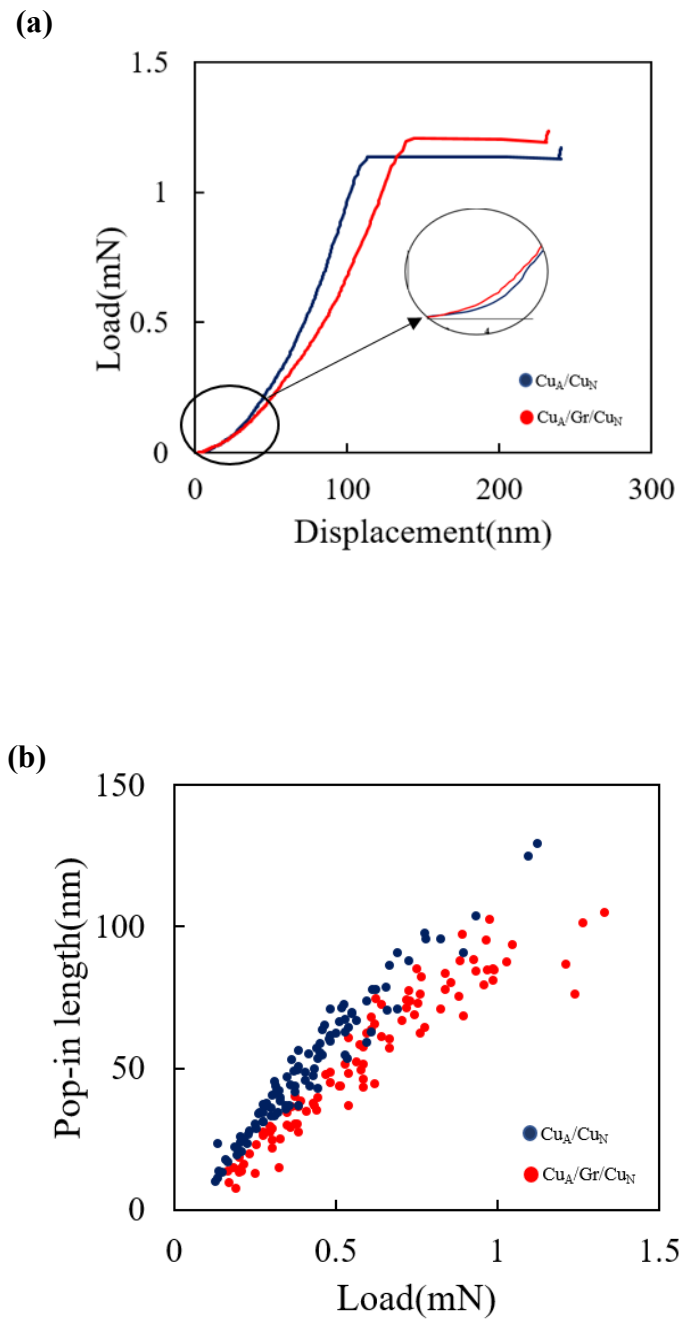
**Fig. 5.** SEM micrograph showing a series of indent inside a CuA grain, sufficiently remote from grain boundaries to avoid plastic interactions.



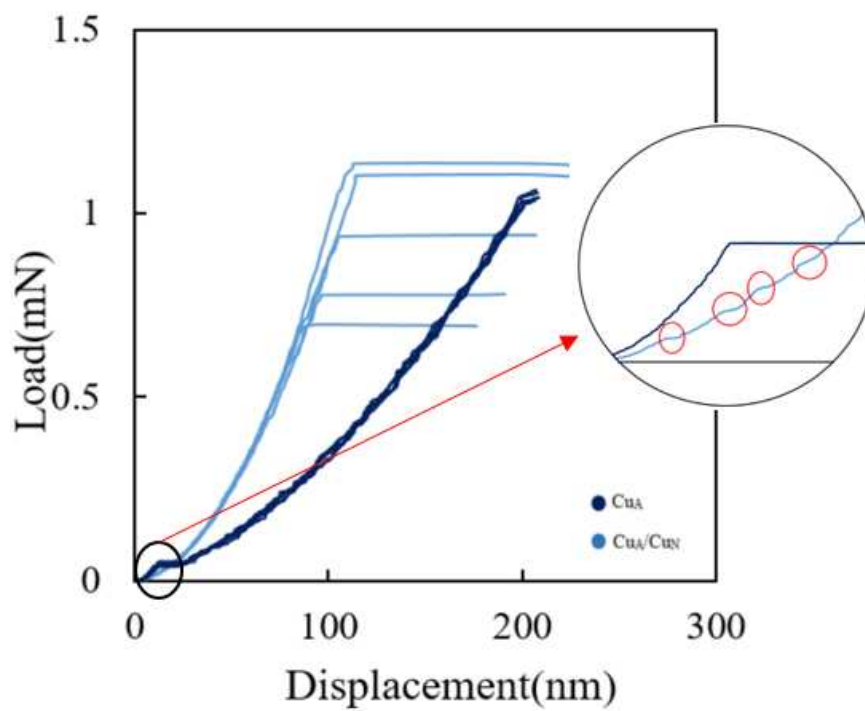


**Fig. 6.** (a) Comparison of load-penetration curves for  $\text{Cu}_A$  and  $\text{Cu}_A/\text{Gr}$  in load-control mode; (b) comparison of load-penetration curves for  $\text{Cu}_A$  and  $\text{Cu}_A/\text{Gr}$  in displacement-control mode; (c) first and second pop-ins in  $\text{Cu}_A$  system; (d) first, second, and third pop-ins in  $\text{Cu}_A/\text{Gr}$  system; (e) comparison the length of first and second pop-ins of  $\text{Cu}_A$  with first, second and third pop-ins of  $\text{Cu}_A/\text{Gr}$  in load-control mode; (f) comparison the first pop-in length vs load of  $\text{Cu}_A$  and  $\text{Cu}_A/\text{Gr}$  in load-control mode; (g) comparison the first pop-in length vs load of  $\text{Cu}_A$  and  $\text{Cu}_A/\text{Gr}$  in displacement-control mode; (h) comparison of probability function vs load of  $\text{Cu}_A$  and  $\text{Cu}_A/\text{Gr}$  in load-control mode; (i) comparison of probability function vs load of  $\text{Cu}_A$  and  $\text{Cu}_A/\text{Gr}$  in displacement-control mode.

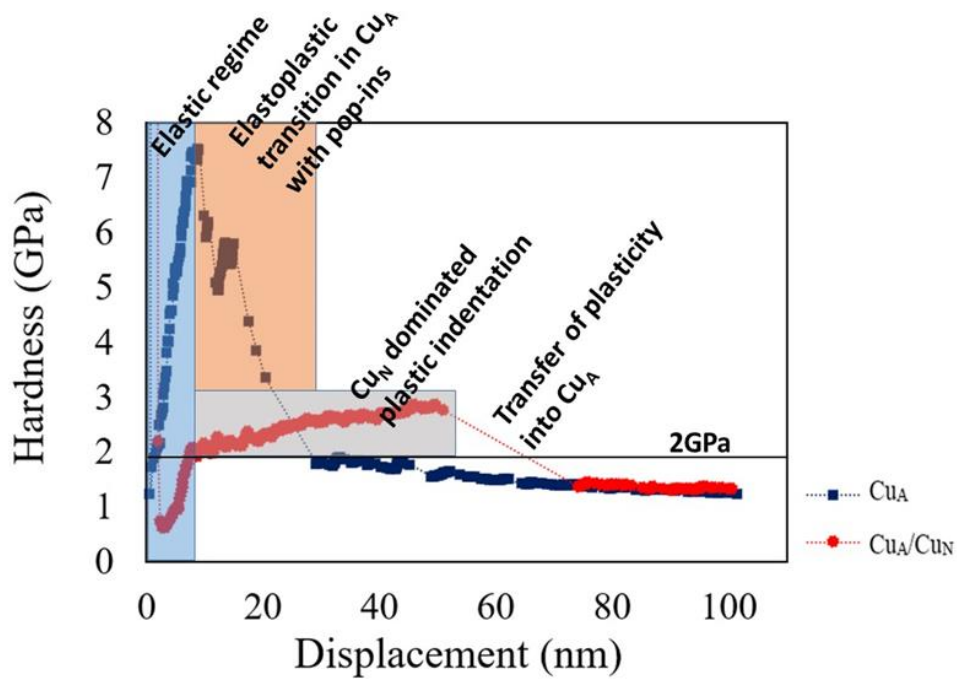




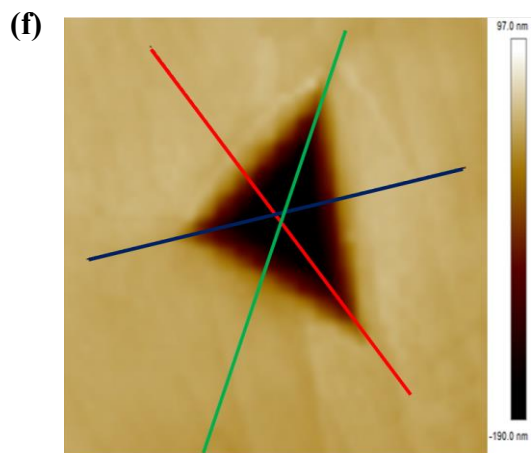
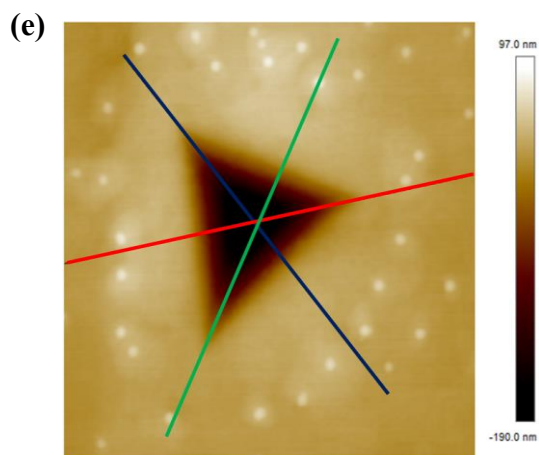
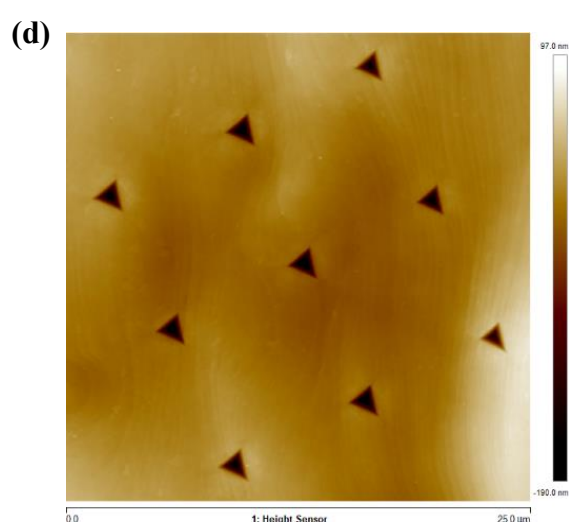
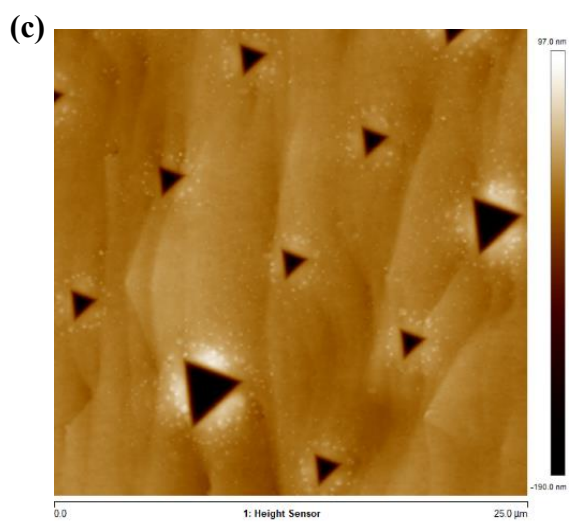
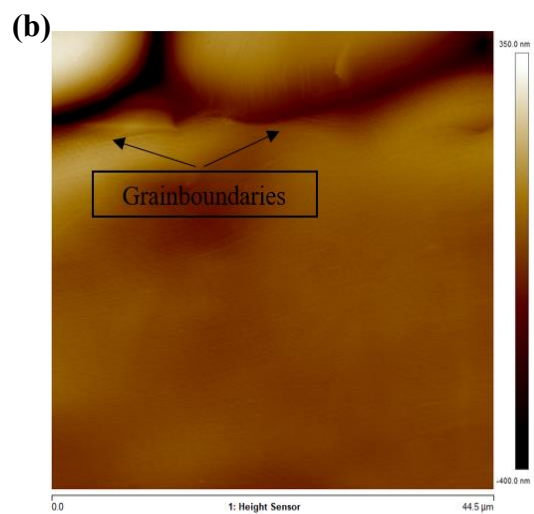
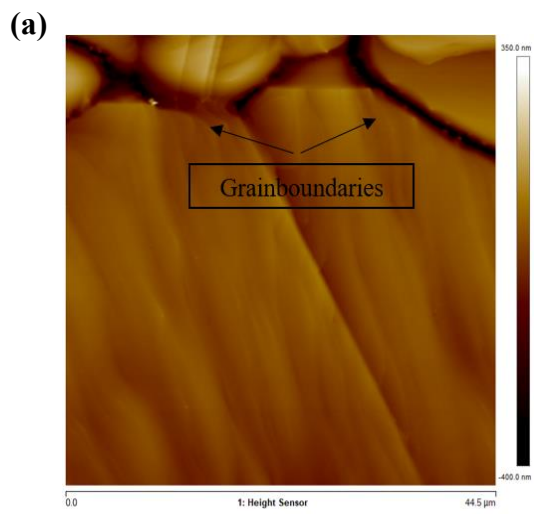
**Fig. 7.** (a) Comparison of the load-penetration curves for  $\text{Cu}_A/\text{Cu}_N$  and  $\text{Cu}_A/\text{Gr}/\text{Cu}_N$  in load-control mode; (b) comparison of the first pop-in length of  $\text{Cu}_A/\text{Cu}_N$  and  $\text{Cu}_A/\text{Gr}/\text{Cu}_N$  in load-control mode.



**Fig. 8.** Comparison of pop-in length for  $\text{Cu}_A$  and  $\text{Cu}_A/\text{Cu}_N$ . The inset shows the small pop-ins in one of the curves which occur before the first large pop-in in  $\text{Cu}_A/\text{Cu}_N$ .



**Fig. 9.** Variation of hardness as a function of penetration depth for Cu<sub>A</sub> and Cu<sub>A</sub>/Cu<sub>N</sub>, showing the significantly larger hardness of before Cu<sub>N</sub> before the plasticity is transferred into the underlying Cu<sub>A</sub> layer with the hardness following then the trend obtained for a single Cu<sub>A</sub> film.



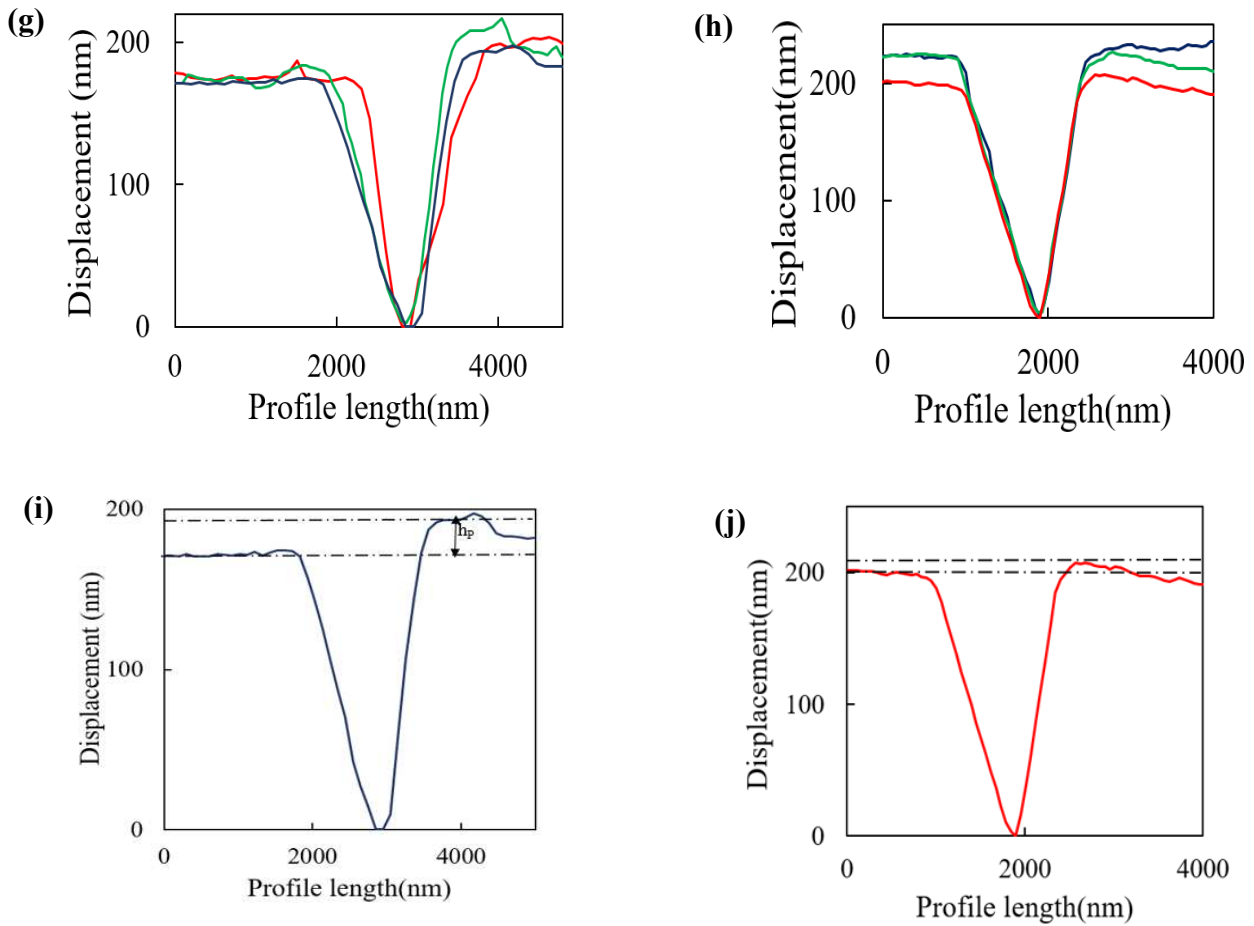


**Fig. 10.** (a) AFM image before indentation on  $\text{Cu}_A$  (size of the square box is  $44.5 \times 44.5 \mu\text{m}^2$ ); (b) AFM image before indentation on  $\text{Cu}_A/\text{Gr}$  (size of the square box is  $44.5 \times 44.5 \mu\text{m}^2$ ); (c) AFM image after indentation on  $\text{Cu}_A$  (size of the square box is  $25 \times 25 \mu\text{m}^2$ ); (d) AFM image after indentation on  $\text{Cu}_A/\text{Gr}$  (size of the square box is  $25 \times 25 \mu\text{m}^2$ ); (e) higher magnification of one indent on  $\text{Cu}_A$ ; (f) higher magnification on one indent on  $\text{Cu}_A/\text{Gr}$ ;  $\text{Cu}_A$ ; (g) three height profiles across the indent shown in (e); (h) three height profiles across the indent shown in (f); (i) height profile (dark blue) across the indent shown in (e); (j) height profile (red) across the indent shown in (f).

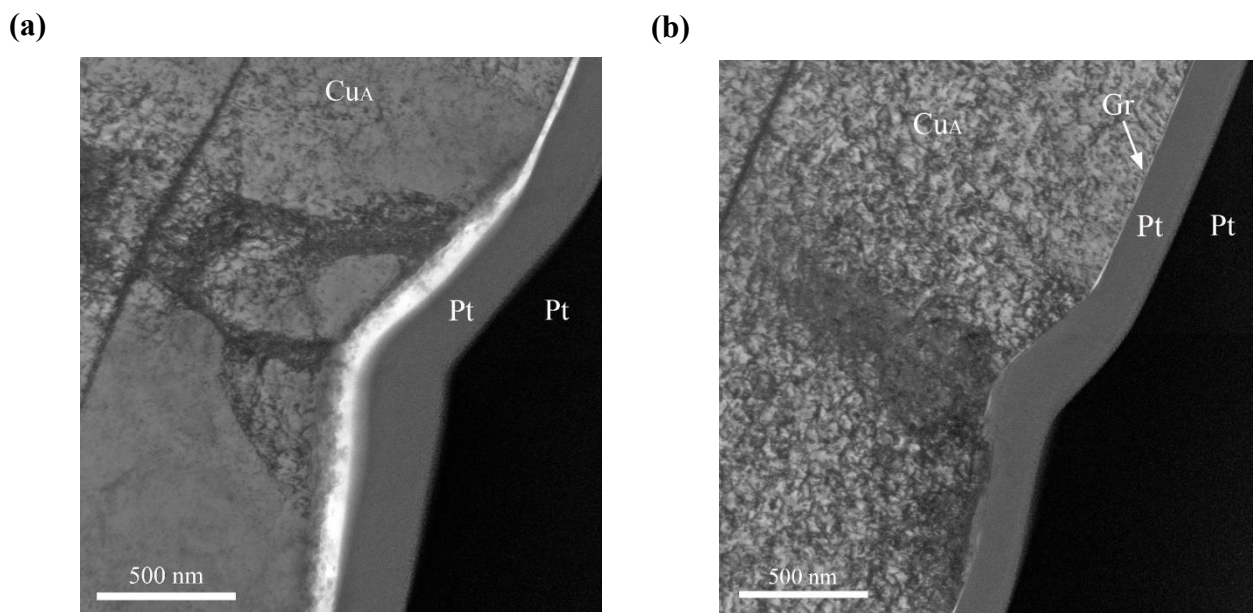


**Fig. 11.** (a) TEM micrograph showing the dislocation arrangements in Cu<sub>A</sub>; (b) TEM micrograph showing the dislocations structures in the Cu<sub>A</sub>/Gr system. The two top layers consist of successively deposited electron beam Pt layer and ion beam Pt layer from the left to the right side, respectively.

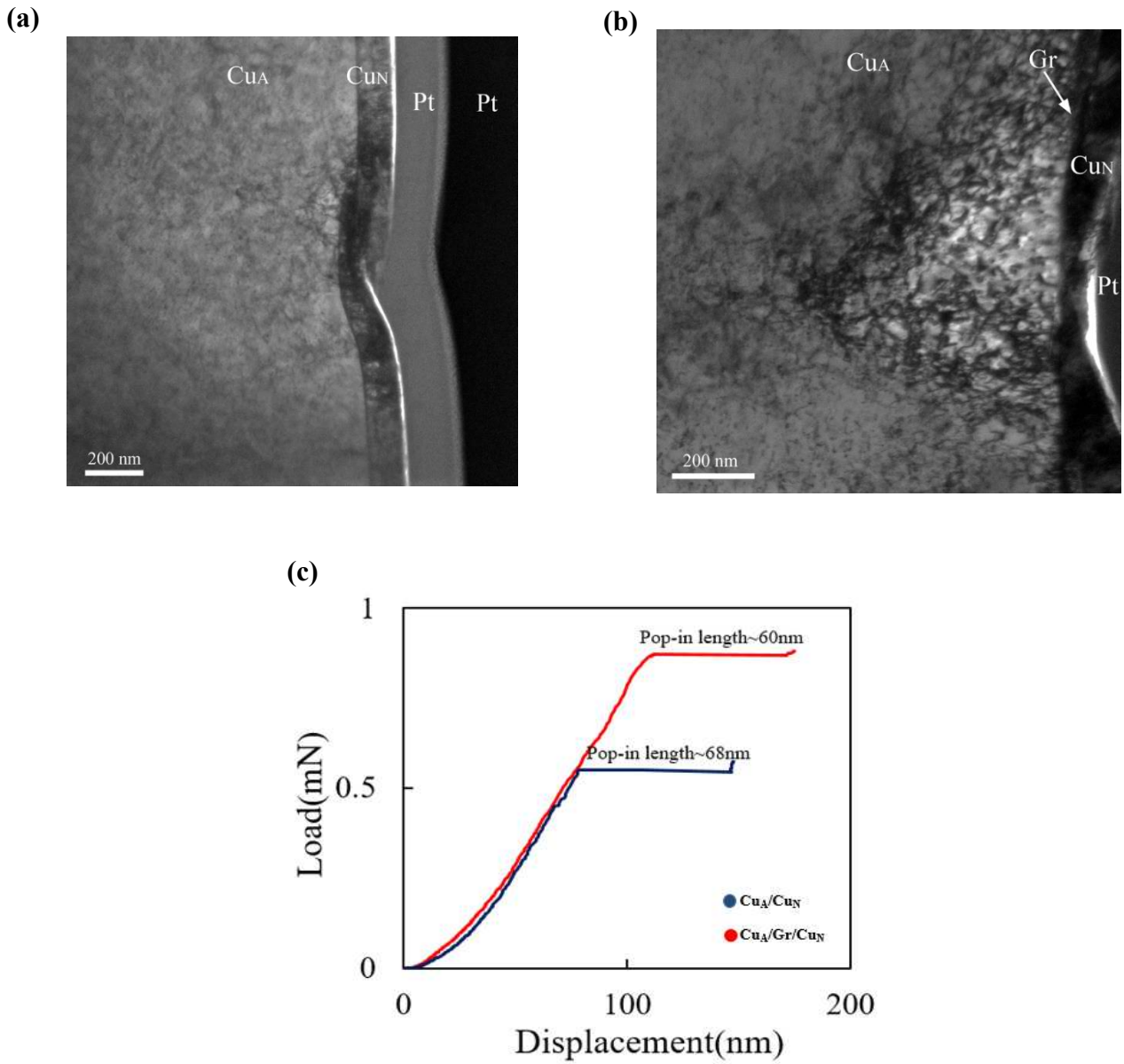


**Fig. 12.** TEM micrograph showing the dislocation structure under a 100 nm-deep indent in the Cu<sub>A</sub>/Cu<sub>N</sub> film; (b) TEM micrograph showing the dislocation structure under a 100 nm-deep indent in the Cu<sub>A</sub>/Gr/Cu<sub>N</sub> film; (c) comparison of the load-penetration curves for Cu<sub>A</sub>/Cu<sub>N</sub> and Cu<sub>A</sub>/Gr/Cu<sub>N</sub> under load-control mode.

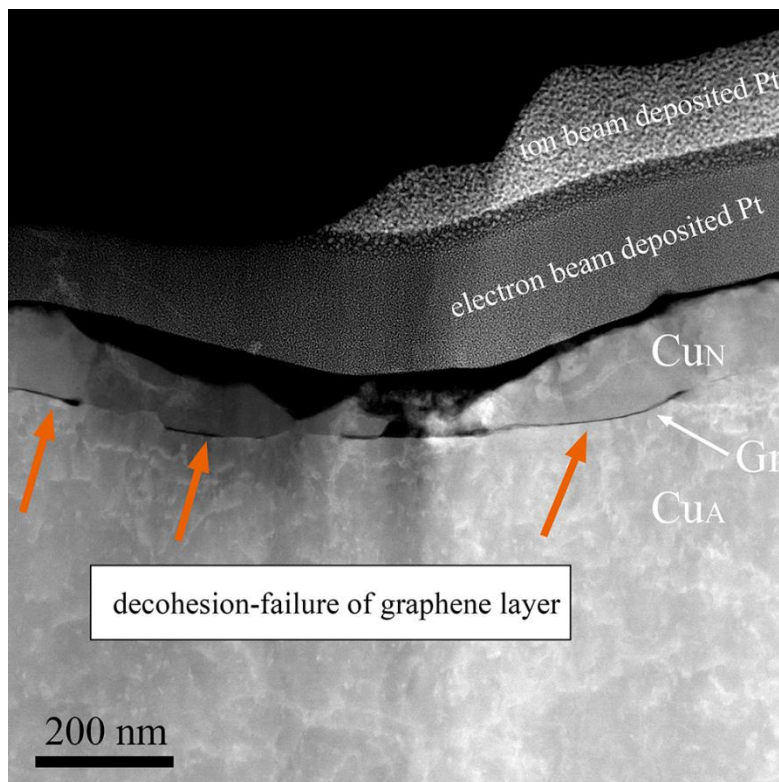


**Fig. 13.** HAADF STEM micrograph of the region below an indent performed in a Cu<sub>A</sub>/Gr/Cu<sub>N</sub> system exhibiting decohesion/failure at the graphene layer level.



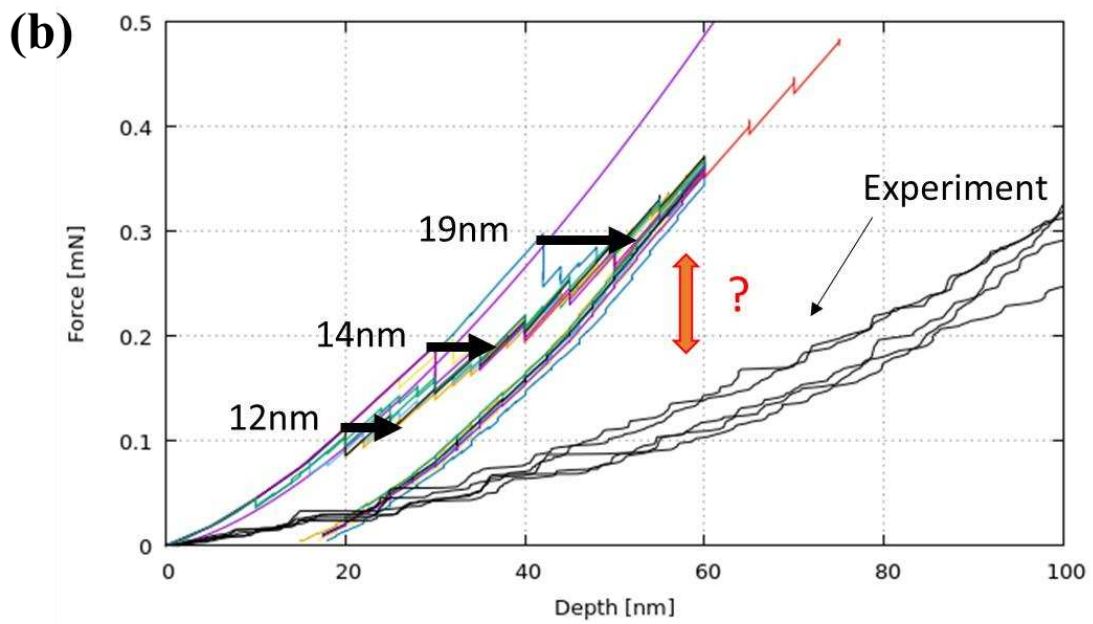
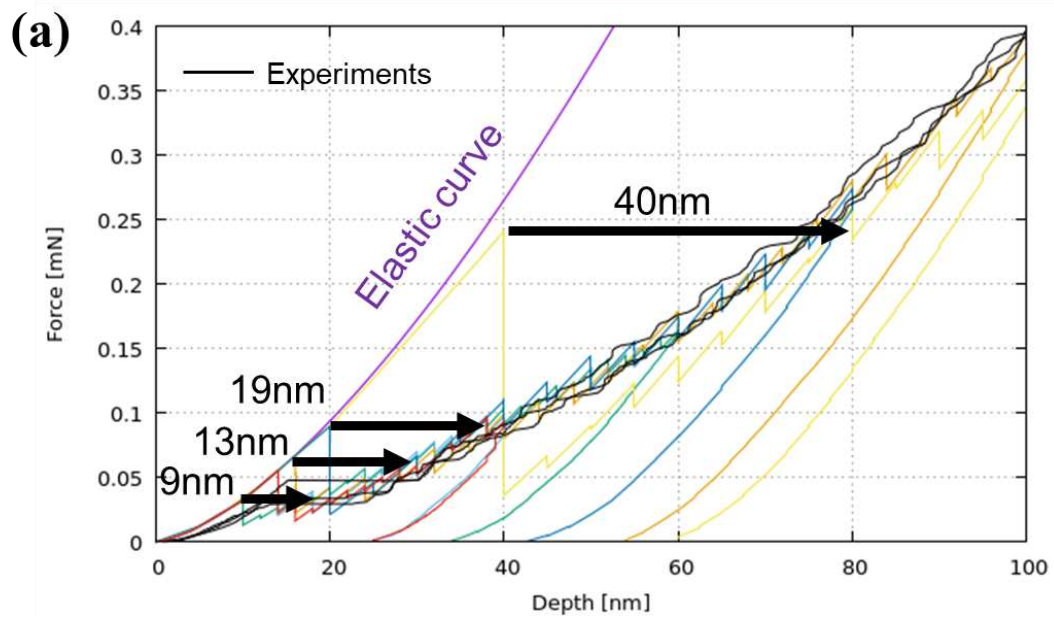


**Fig. 14.** (a) DDD predicted load-penetration curve for  $\text{Cu}_A$  for the different onset of the nucleation algorithm; (b) DDD load-penetration curve for  $\text{Cu}_A/\text{Gr}$ , which shows a stiffer mechanical response.

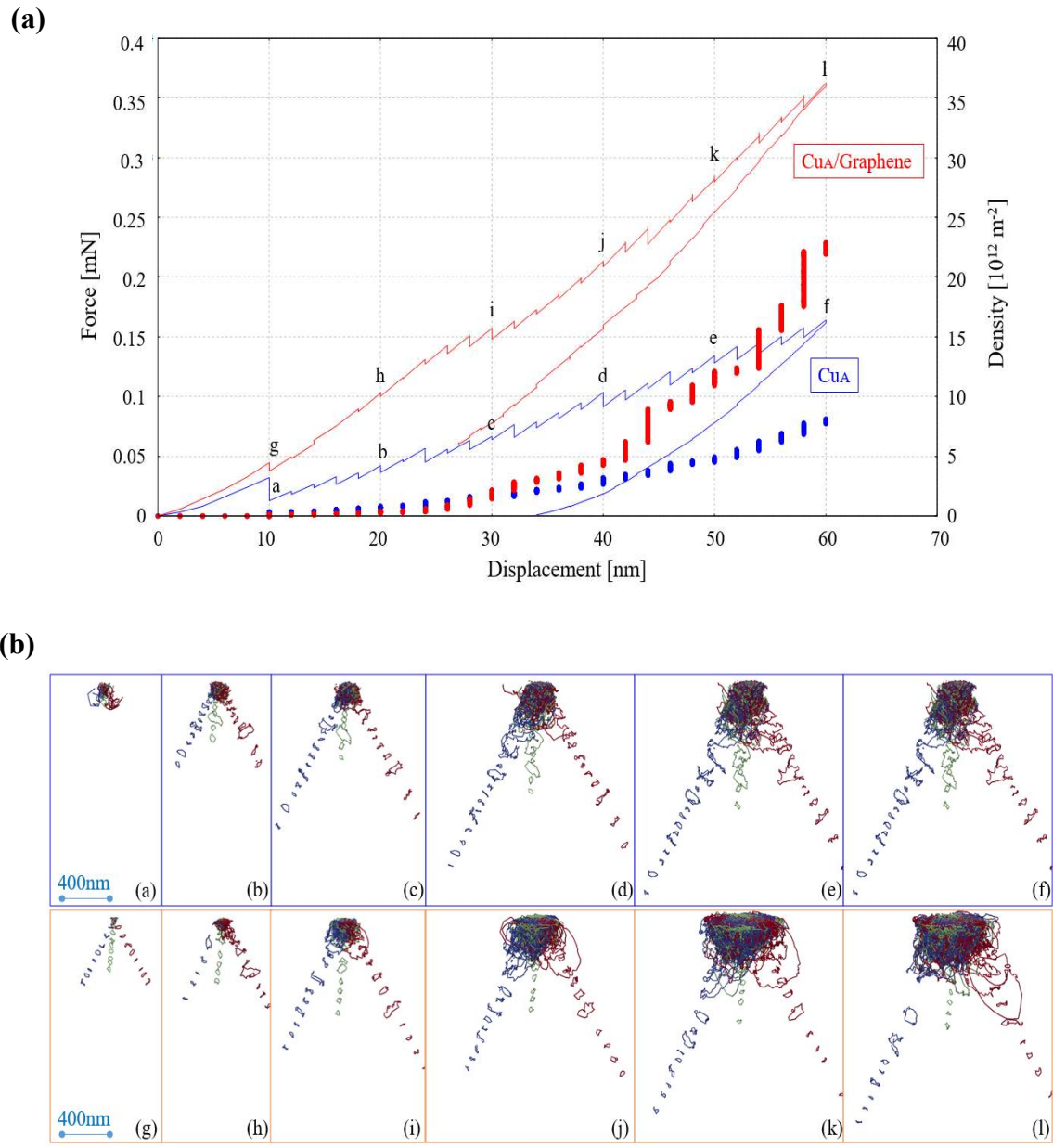
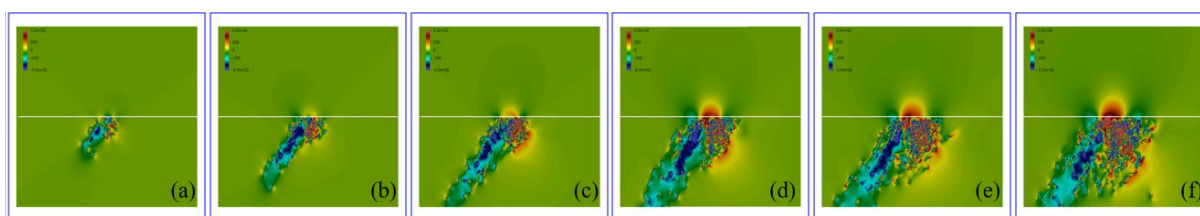


**Figure 15.** (a) DDD load-penetration curve and evolution of dislocation density (filled circles) for  $\text{Cu}_A$  and  $\text{Cu}_A/\text{Gr}$  when plasticity is triggered at 10 nm depth; (b) dislocation arrangements for  $\text{Cu}_A$  and  $\text{Cu}_A/\text{Gr}$  at different instants of indentation as indicated on the load-penetration curve.

(up)



(down)

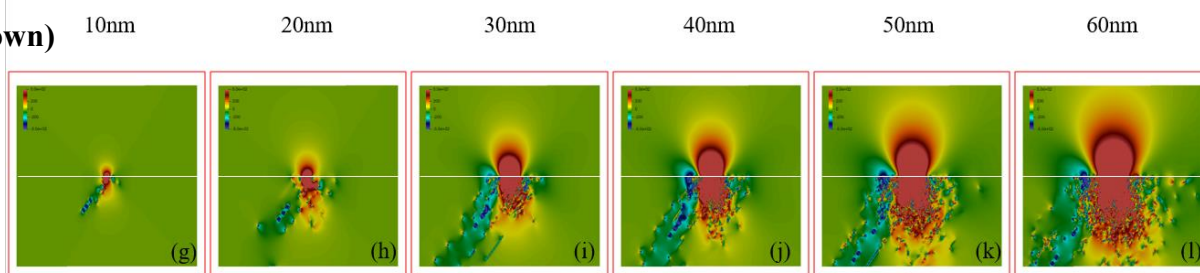
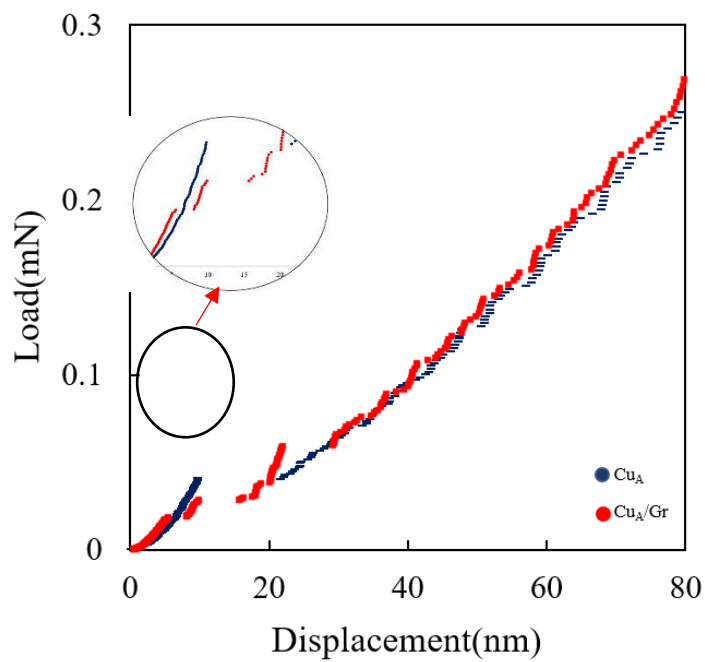
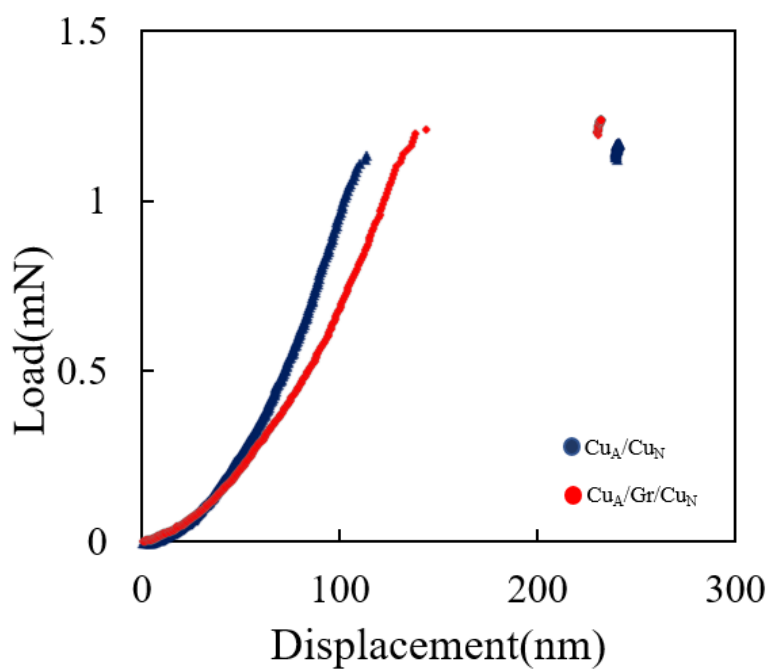


**Figure 16.** Evolution of the normal stress  $n^T \cdot \sigma \cdot n$  with  $n=(111)$  for different indentation depths inside (up) Cu<sub>A</sub>, (down) Cu<sub>A</sub>/Gr; the color range is within [-500MPa:500MPa]. Note a higher long-range normal stress zone in Cu<sub>A</sub>/Gr.



(a)



(b)

**Figure A1** (a) Comparison of representative force-penetration curves for  $\text{Cu}_A$  and  $\text{Cu}_A/\text{Gr}$ ; (a) Comparison of representative force-penetration curves for  $\text{Cu}_A/\text{Cu}_N$  and  $\text{Cu}_A/\text{Gr}/\text{Cu}_N$ .